MASTER'S THESIS

SURFACE PREPARATION FOR ELECTRON BACKSCATTER DIFFRACTION INVESTIGATION USING LOW ENERGY ARGON AND HIGH ENERGY FOCUSED GALLIUM ION BEAMS

KITTI RATTER
Physics MSc., Condensed Matter Physics Specialization Module

SUPERVISOR:
KÁROLY HAVANCSÁK CSC.
docent

EÖTVÖS LORÁND UNIVERSITY
Department of Materials Physics

2012

Acknowledgments

As I begin this section at the end of these very productive and special two years, it occurs to me that I have quite a long list of people to whom I owe my gratitude.

First of all, I would like to thank my supervisor, Dr. Károly Havancsák for his guidance and support in the past two years. It is an understatement to say that I learnt a lot as his student. I also thank him for thoroughly reading my thesis many times, and giving me useful suggestions. I would like to take the opportunity here, on behalf of myself and my colleagues, to thank him for his hard work in making our laboratory productive and competitive. I feel very lucky that I could work under his supervision.

I would also like say thank you to Dr. János Lendvai, the leader of this project, for giving me the chance to take part in this project, and for following and supporting my work.

I thank Dr. Groma István, the head of the Institute of Physics and the Department of Materials Physics for giving me the opportunity to be the part of the department, and also taking interest in my work.

The past two years would not have been what they were without my colleagues, Dr. Zoltán Dankházi and Gábor Varga. Zoltán helped me with countless things during my time at the laboratory, ranging from computer aid to the most naive questions about physics. He also helped me in my measurements and in understanding how EBSD works. I thank him for all of these and for his recommendations on my thesis. I am going to miss our lunches, the silly Fridays, and of course the French lessons.

I owe many thanks to Gábor. He worked overtime many times when I needed to study for exams, as well as helping me in my work. He not only performed many measurements, but gave very useful suggestions and remarks. Besides his knowledge of science, his never ending patience, sense of humor and good taste in music made him a great person to work with.

I thank Zsolt Rádi and Dezső Szigethy, the technical and managing directors of Technoorg Linda Ltd. Co. for starting and implementing this cooperation, I certainly hope it will be continued.

I thank Gyula Vincze from Technoorg Linda Ltd. Co. for the preparation of the samples.

Special thanks to Zoltán Bakai from whom we learnt how to use the Gentle Mill,

and whom we could call anytime we had problem or question. His work is very much appreciated.

From the university, I owe thanks to Dr. Jenő Gubicza and Zoltán Hegedűs for the silver samples and their help in explaining a result.

I owe my gratitude to Dr. Gøran Jan Nilsen for helping me every step of the way in the past two years. I thank him for the strength he gave me when I needed to work hard, for the very reason to work for and for his patience when it was needed. He read this thesis not once and corrected my mistakes, gave suggestions. I learnt English for science from these corrections and everyday English from our daily conversations. I got my second language from him. Tusen takk for alt min Nilsen Bamsefar.

My greatest gratitude is for my parents. They were supporting me for more years than I would like to admit. Without them I wouldn't be the person I am now (in fact, I would not be a person at all). I'm sure I will not be able to thank them for their work no matter how hard I try, instead I will do my best to make them proud.

The Project is supported by the European Union and co-financed by th European Social Fund (grant agreement no. TAMOP 4.2.1/B-09/1/KMR-2010-0003).

Contents

1 Introduction **1**

2 Methods and Equipment **5**

2.1 FEI Quanta 3D FEG Dual-Beam Scanning Electron Microscope 5

2.2 Gentle Mill 3 12

2.2.1 Simple Models of Ion Sputtering 15

2.3 Electron Backscatter Diffraction 19

2.3.1 Theory of EBSD 19

2.3.2 Instrumentation of EBSD and Data Processing 27

3 Measurements **38**

3.1 Measurements Using Focused Ion Beam 40

3.2 Measurements Using Low Energy Argon Ion Beam - Gentle Mill 45

3.2.1 Polishing Method and Other Considerations 45

3.2.2 Time Dependence 47

3.2.3 Angle Dependence 49

3.2.4 Results and Discussion of EBSD Measurements 49

4 Conclusion **57**

A Appendix **58**

B Appendix **62**

"If you can see, look.
If you can look, observe"
(Book of Exhortations)

"When you have eliminated all which is impossible,
then whatever remains, however improbable, must be the truth."
(Sir Arthur Conan Doyle: The Case-Book of Sherlock Holmes,
The Adventure of the Blanched Soldier)

1 Introduction

Much of the solid material that surrounds us has crystalline structure (metals, minerals, composites, etc.). In the bulk, these materials are usually polycrystalline, meaning that they are built up by smaller monocrystals referred as grains.

The orientations of these grains are in the most cases not randomly distributed, rather there are preferred orientations, or orientation patterns, this is referred to as the texture of the material. The microtexture is very important because many properties of the material depend on it, for example: the Young's modulus, the Poisson's ratio, strength, toughness, magnetic permeability, electric conductivity and thermal expansion. The microtexture is not static, but depends on what the material has been through (induced stress, heat, etc.). Therefore it is crucially important to investigate the microtexture of the material. This requires finding a suitable probe. Radiation of some sort is commonly used, as it can penetrate into or through the sample and yield structural information on it.

	Light	Neutrons	X-Rays	Electrons
Wavelength (nm)	400-700	0.05-0.3	0.05-0.3	0.001-0.01
Energy (eV)	1	10^{-2}	10^{4}	10^{5}
Charge (C)	0	0	0	-1.602×10^{-19}
Rest mass (g)	0	1.67×10^{-24}	0	9.11×10^{-28}
Penetration depth	-	10-100	0.01-0.1	10^{-3}

Table 1: *Most common radiations used in materials physics and in solid state physics [1]*

To be able to extract information on the microstructure, the size of the probe has to be on the order of the common size of the microstucture, usually at least one micron. It is obvious that this resolution cannot be obtained by visible light and neutrons cannot be focused sufficiently to a small spot size. X-rays can, in fact, be focused (there exists a technique called μ-XRF), but particle accelerators are needed to produce X-rays for this technique. Typically, a larger volume of the specimen is radiated with neutrons and with X-ray photons, meaning that while macrotexture analysis can be performed, we get no information on the microtexture. We shall use electrons then: they can easily be

focused to a very small spot size using electromagnets and they can diffract like phonons or neutrons [1].

The history of the electron backscatter diffraction (EBSD) started when Kikuchi and his supervisor discovered the electron diffraction pattern, later named after Kikuchi, in 1928 [2]. They were using a 50 keV electron beam on a thin mica film, and the diffraction patterns were recorded by photographic plates. The discovery started an avalanche of work on electron diffraction, and many ended up studying the transmitted as well as the reflected electron diffraction patterns on a large number of materials in different configurations: see Boersch (1937) [3] and Alam (1954) [4]. In 1965 the first commercial SEM appeared on the market, which allowed even faster progress. Venables and Harland were the first to investigate electron backscatter Kikuchi patterns using SEM. In the beginning patterns were detected by a TV camera and later by a phosphorous screen [5]. In 1984 Venables work was continued by Digley, who added the help of a computer for indexing the patterns [6], which proved a major step in the success of modern-day EBSD.

The system which scientists use now dates back to 1993, when Brent Adams introduced the term orientation mapping (OM). Orientation mapping uses the operating principle of the SEM, namely, a well focused electron beam is scanning the surface of the sample and products are being collected and being displayed at each point. The products in this case are diffraction patterns produced by backscattered electrons, which are indexed automatically by the computer, resulting in colour being displayed on the screen according to the orientation of the grain found at that specific point of the specimen [7].

The EBSD technique is a very young technique and a very challenging one in that sense that it requires major computing capacity, or before that was available, major human power for the indexing of each pattern. Just for the sake of comparison, using the first computer-aided indexing, the operator had to select three lines at each pattern, before the indexing could be done by the computer. The orientation maps to be shown in this work consist of $200 \times 200 = 40000$ points. If we assume indexing one point takes 5 seconds on average, one map would take 200000 seconds = 56 hours to produce. These days we are lucky in that powerful computers and well written algorithms are available to reduce the duration of one mapping (as mentioned above) to less than 15 minutes. However, we should remember that what we can do now by just one click,

others worked for for years (not only in the case of EBSD).

The crucial part of the sample for the purpose of the EBSD investigation is the surface, since the information we get comes from the upper 10 nanometer thick region of the specimen. The surface has to be perfectly clean, there cannot be an amorphous covering on it. If there is, either no or a faded diffraction pattern is recorded. Besides, it has to be effectively smoothed, because of shadowing effects. The usual diamond polishing is out of the question, because it can deform the grains on top and this induced stress causes the diffuseness of the diffraction patterns. It has been suggested to polish with colloidal silica for hours. When we attempted this, we could find residual polishing material in the grains of the sample. We also tried to prepare the surface using electropolishing, but we were unable to see any Kikuchi bands.

The requirements for surface quality is very similar to what is expected in the case of a transmission electron microscopy sample, the difference being that only one side of the specimen is important. This similarity gave us the idea to try a device that has proven trustworthy when preparing TEM samples: the Gentle Mill low enery argon ion polisher. This instrument was purposely designed for the final polishing of TEM samples by an internationally successful company, Technoorg Linda Ltd. Co. They provided us with an instrument to try its qualities in this area and if successful, preparing a protocol for fast surface preparation.

Besides probing the properties of Gentle Mill, we also used the built-in focused ion beam system in our microscope. One of the reasons for this was that after surface preparation with the Gentle Mill, the sample had to be moved from instrument to instrument. There can be sensitive samples that do not prefer to be transferred. With an efficient protocol, these samples can be prepared inside the microscope chamber and only stage movements are required before the EBSD investigation can take place.

This work is divided into two parts. In the first part, the instruments and the methods are described. Staring with an introduction to the scanning electron microscopes and focused ion beam systems, pointing out the specifications of our system. In the following chapter, the working principle of the Gentle Mill is described, then a simple model for ion sputtering is given. After the instrument descriptions, the theory of electron backscatter diffraction is reviewed, first with the kinematical theory, then, after realizing that this approximation is not valid, the main ideas of dynamic theory are explained. When the theory is understood, we turn to the actual instrumentation of EBSD

and the details of representing the orientation information.

In the second part, our measurements and results are discussed, starting with the data where FIB was used and finishing with those where Gentle Mill was employed. The conclusion points out our main results and plots our plans for the future.

2 Methods and Equipment

The measurements and sample preparation described in this thesis were performed in the Department of Materials Physics at Eötvös University using a FEI Quanta 3D FEG dual-beam scanning electron microscope (figure 1) and a Gentle Mill 3 low energy ion polisher provided by Technoorg Linda Ltd. Co. (figure 2).

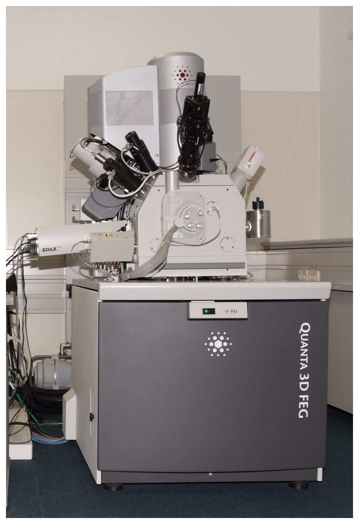

Figure 1: *FEI Quanta 3D FEG dual-beam scanning electron microscope*

Figure 2: *Gentle Mill 3 low energy ion polisher*

2.1 FEI Quanta 3D FEG Dual-Beam Scanning Electron Microscope

In dual-beam electron microscopes, besides the electron source there is an ion source as well. Both beams are suitable for imaging the surface of the sample, but the ion beam is typically used for sputtering or milling. A schematic diagram of a scanning electron microscope can be seen in figure 3.

The electron beam is produced by thermionic field emission (Schottky emission) from a tungsten needle coated with zirconium dioxide (ZrO_2) and is then accelerated to an energy chosen by the user $(2\ keV$-$30\ keV)$ by an electric field, before being focused by condenser lenses to a spot on the specimen. The diameter of the beam as measured on the sample is about 1 nm, depending on the voltage, current and the time elapsed since the last adjustment. The beam passes through pairs of scanning coils, which deflect the beam in the x-y plane so that it scans in a raster fashion over a rectangular area of

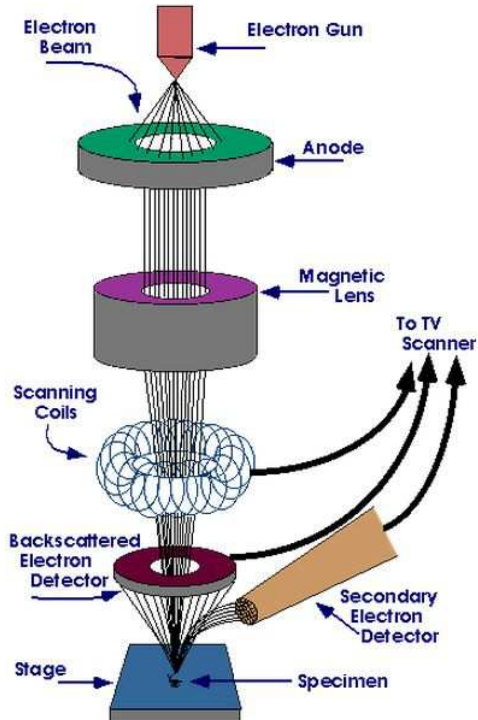

Figure 3: *A schematic diagram of a scanning electron microscope [8]*

the sample surface. The electron gun and the column where the beam is accelerated and formed must be under high vacuum $(10^{-7}\ Pa)$. In conventional scanning electron microscopes the sample chamber is also under high vacuum, however the FEI Quanta 3D FEG can also be used in low vacuum and ESEM (environmental scanning electron microscope) mode, where the H_2O pressure can vary between $40\ Pa$ and $2700\ Pa$. The temperature of the stage is adjustable as well to allow to work in 100% humidity. The measurements described in this work were preformed in the conventional high vacuum mode and so no further details on ESEM mode will be given here.

While the beam is scanning the surface, various particles (electrons, photons) are emitted at each point (figure 4). These particles can be detected by specialized detectors (see below) resulting in a pixel being displayed on the screen with a brightness according to the quantity of the generated particle. Thus, microscopic images can be made by a scanning electron microscope. Since only the intensity is measured, these images will be represented on a grayscale (figures 5).

In the case of a traditional scanning electron microscope, bulk specimens are usually

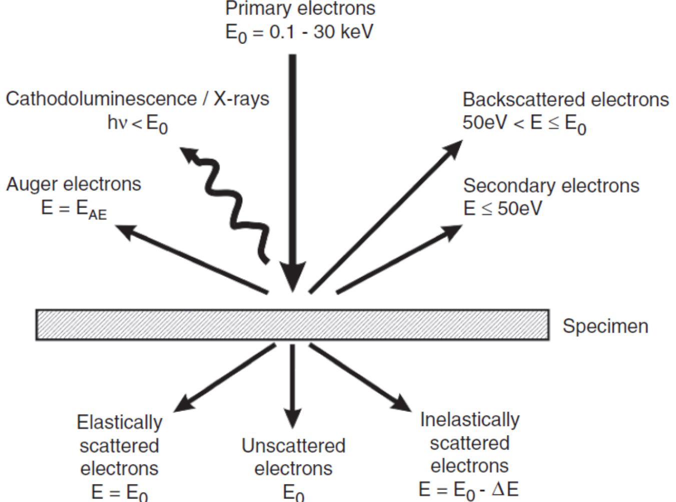

Figure 4: *Products generated from electron beam - specimen interaction; E_0 is the energy of the incident beam. Different products are generated in different volumes of the sample. This fact gives a natural limit for the resolution [9].*

investigated and the electron beam cannot penetrate through the sample because of its thickness. Only those products can be detected that are generated on the excited surface of the sample.

In this context, the scanning transmission electron microscope (STEM) has to be mentioned. In this case, a very thin $(< 100nm)$ sample is placed on a specific sample holder and a detector is placed under the sample to detect the transmitted products.

We can detect the three main products generated by the electron beam on the upper surface of the sample:

- Secondary electrons (SE): secondary electrons are ejected from the the specimen atoms by inelastic scattering. Their energy is low: $< 50\ eV$, with a broad spectrum, with mean energy value of $3\ eV$-$5\ eV$. They originate from a small volume $(few\ nm^3)$ and therefore the highest resolution can be reached by using these for imaging. The generated SE intensity depends on the angle between the electron beam and the vector normal to the surface, hence using SE images the surface morphology can be observed (left image on figure 5). The most common secondary electron detector is the Everhart-Thornley detector (ETD). Three main parts of the detector are: a Faraday cage with a positive bias to attract the low

energy SEs; a scintillator inside the cage to convert electrons to photons; and a photomultiplier to amplify the signal. The application of a biased Faraday cage and a photomultiplier provides fast (broadband) imaging and it has good vacuum tolerance. Prior to the ETD, taking a SE image took hours, ever since it only takes a couple of seconds.

- Backscattered electrons (BSE): backscattered electrons are elastically scattered electrons from the primary beam. The BSE intensity depends on the average atomic number of the area where they are reflected from, the higher the atomic number, the higher the intensity. Thus a BSE image shows atomic number contrast. The differences between the SE and the BSE image can be observed in figures 5. BSE detectors are usually semiconductor devices divided into 2 or 4 segments and placed in the direction of the primary beam, surrounding it (see figure 3). It is also possible to measure the diffraction of the backscattered electrons. This method is called Electron Backscatter Diffraction (EBSD). (See the details below.) The detector used in our microscope for EBSD investigation is called a Hikari camera and consists a phosphorous screen and a high resolution CCD camera.

- X-rays: in the interaction between the electron beam and the sample, X-ray photons are also produced. The primary electron beam may excite an electron in an inner shell, ejecting it from the shell while creating an electron hole where the electron was. An electron from an outer, higher-energy shell can fill this hole and the energy difference between the two shells may be released as an X-ray photon. The energy differences between the shells and thus the energy of the emitted X-ray photon is characteristic of the emitting element and therefore compositional measurements can be performed. For the energy dispersive detection of the X-ray photons a high purity silicon single crystal analyzer is used. Since it does not contain lithium, the cooling of the analyzer is not so crucial. To decrease the noise however, it is necessary to cool it down to $-60°C$ using Pertier cooler.

As mentioned above, the dual-beam electron microscope does not contain only an electron gun, but an ion gun as well. The so called FIB (focused ion beam) system allows the user to remove small volumes of the sample, which can be useful when for

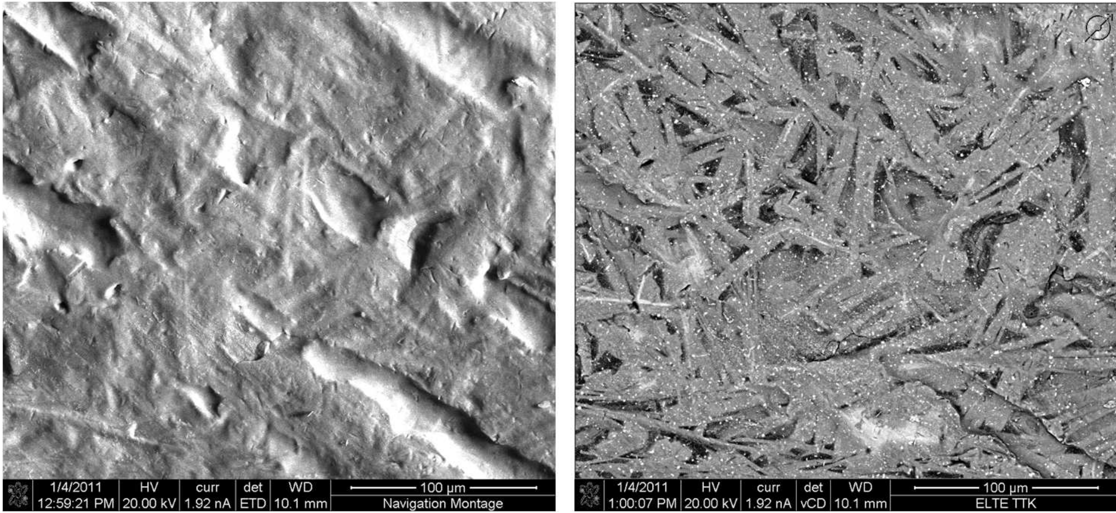

Figure 5: *Secondary electron image and backscattered electron image (respectively) obtained on the same area of an MgCuNiY alloy (sample was prepared by Ádám Révész, image was taken by Gábor Varga)*

eg: the area of interest is a cross-section of the sample; samples for TEM investigation are to be prepared; and (as is shown later), preparation of certain surfaces for EBSD investigation.

The FIB system is very similar to the SEM system; it consists of a liquid metal ion source, which is a tungsten needle attached to a tungsten reservoir, where the gallium is stored. An empty liquid ion source is shown in figure 6 and a schematic of the gun is shown in figure 7. It is possible to use a different metal in an FIB system but the most common choice is gallium, because it has a very low melting point $(29.8°C)$, is viscous enough, does not react with the tungsten and has very good super-cooling properties; after it is melted, it stays liquid for weeks under ambient conditions.

The gallium is heated by the coil heaters and then it flows and wets the tungsten needle when it is in the liquid state. At the tip of the needle an electric field, the so called extractor voltage, ionizes the liquid gallium and a Ga^+ current results. The accelerating voltage in the ion column can be adujted by the user $(1\ kV\text{-}30\ kV)$. As it has been described before about the electron gun, the beam is shaped and focused by magnetic lenses and scans the surface in a fashion given by the pattern to be milled (rectangular or circular). The diameter of the ion beam on the surface is in the order of a few nm.

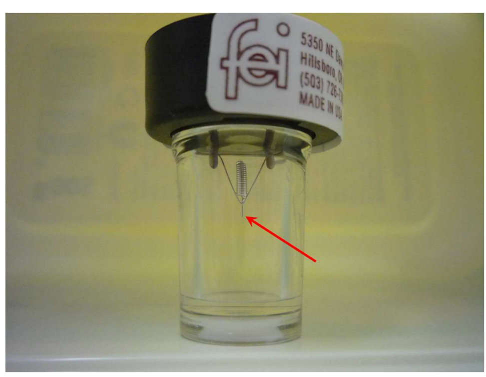

Figure 6: *Empty liquid metal ion source, the spiral was filled with gallium (our photo)*

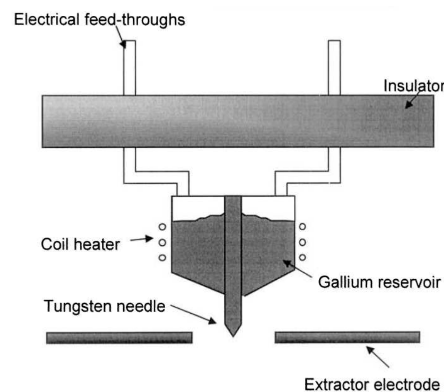

Figure 7: *Schematic diagram of the liquid ion source [10]*

Where the beam strikes the surface of the sample sputtered atoms, molecules, secondary electrons and secondary ions are emitted [10].

As in case of electron beam, the secondary electrons and the secondary ions can be used for imaging. During the interaction, the incident ion loses its energy and, if not backscattered, will come to rest below the specimen surface. The penetration depth of the incident ion varies with the energy, the angle of incidence and the material. Tables can be found in literature, typical value are in the range of $100\ nm$. In other words, the surface, where the focused ion beam was applied is damaged.

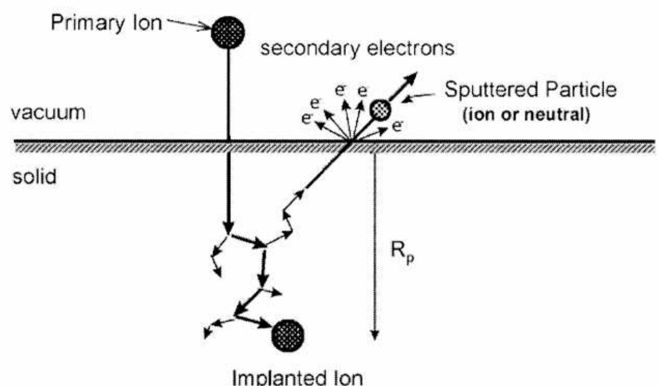

Figure 8: *A schematic diagram of the sputtering process and penetration of the sample by the ion [11]*

Besides the implantation of gallium, there are several artifacts of the ion milling. The ion bombardment generates a collision cascade in the surface region of the sample and the atoms are displaced from their equilibrium positions, as a result of which amorphous phases occur. The thickness of this phase strongly depends on the material. The more complicated and larger the unit cell, the stronger the amorphisation. A good example of this can be found in the work of T. L. Matteson et al. [12], where the authors compared the FIB induced amorphisation of silicon (diamond structure with lattice parameter $0.543\ nm$) and copper (fcc with lattice parameter $0.361\ nm$). They observed that copper, in fact, does not amorphize at all, but rather Cu_3Ga phase forms at certain crystallographic directions.

Another artifact of the FIB milling is the redeposition of the removed material. One has to take this into account before starting the milling and space has to be prepared for the redeposited material, to avoid the covering of the area of interest [11]. An interesting effect shown in reference [12] is that even the redeposited copper nucleates more or less epitaxially with the Cu substrate.

FIB systems exist as single columns, but combining with SEM has many advantages. The motivation for building both in one system was to avoid having two separate tools for sample preparation and imaging. To remove the sample from one and transport it to the other, finding the area of interest, is rather inconvenient.

There are several configurations, the most typical (as in our system) configuration consists of a vertical electron column and an ion column at 52 ° tilt. To mill normal to the surface the sample needs to be tilted. The vertical position of the specimen can be chosen such that the area of interest is in the intersection of the two beams (figure 9). This not only allows us to observe the process of the milling, but the cross section of the sample can be imaged and analytical (X-ray) measurements can be preformed without any sample movement.

Without aiming to give a complete list of techniques, dual-beam systems make it convenient to investigate cross sections, 3D tomography can be preformed by slicing and measuring (imagining or X-ray) repeatedly, samples for TEM investigation can be fabricated, surfaces for EBSD investigation can be prepared. The list can be continued and basically the only limit is one's imagination [13].

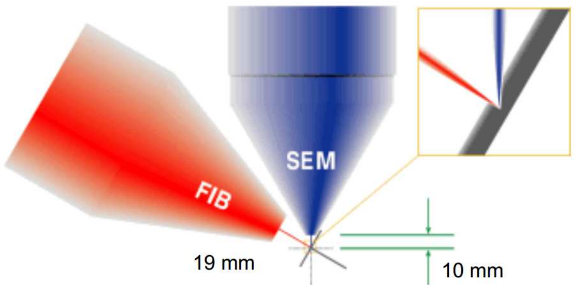

Figure 9: *Vertical SEM and FIB at 52°. The area of interest can be positioned at the intersection of the two beams, allowing real-time monitoring of the milling. The typical working distances (distance between the exit of the columns and the sample surface) are also shown in the figure [13].*

2.2 Gentle Mill 3

The Gentle Mill is an instrument designed by Technoorg Linda Ltd. Co. for the final polishing of samples prepared for transmission microscopic investigation. The damaged amorphous layer from the TEM sample surface is removed by using a low energy $(100\ eV\text{-}2\ keV)$ argon ion gun with a tiltable sample holder.

Since the EBSD method is also very sensitive to the surface quality it was decided to try the Gentle Mill's capabilities for preparing sample surfaces for EBSD investigation. To aid this, a special sample holder was prepared by Technoorg Linda Ltd. Co. for bulk samples.

A schematic diagram of the low energy ion gun is shown in figure 10. The electron and ion trajectories in figure 10 were determined by computer simulation. Electrons are ejected from the hot ring cathode (2) and because of the opposing electrostatic field they are reflected by the front side cold cathode system (5). Thus, electrons are oscillating between the backside (1) and the front side cathode systems (5), which results in a high electron density around the axis of the anode (4). The trapped electrons produce ions by interacting with the argon gas in the gun. The positively charged ions are accerelating toward the cold cathodes producing more electrons by striking them, which further increases the electron and hence, ion density. The front side cold cathode is combined with electrostatic lenses and these have two functions: focusing the beam onto the sample and acting as an energy filter. Ions with lower energy than the focusing energy are

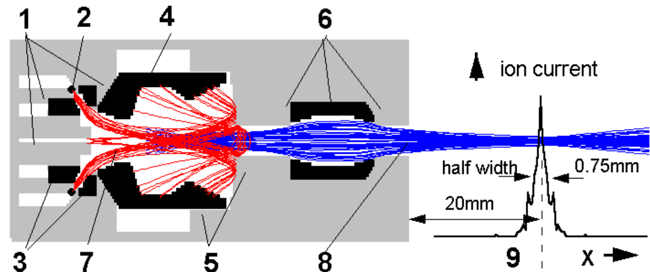

Figure 10: *A schematic diagram of the low energy ion gun; 1-Backside cold cathode system, 2-Hot ring cathode, 3-Adjusting electrode, 4-Anode, 5-Front side cold cathode system, 6-Focusing lens, 7-Electron trajectories (red), 8-Ion trajectories (blue), 9-Ion current density distribution [14]*

reflected back to the source. Thus the energy of the ion beam is defined by the focusing potential (lowest energy) and the anode potential (highest). As the calculated energy distribution on figure 12 shows, the average energy of the ion beam is at 85%-90% of the anode potential. The Gentle Mill is not a highly focused beam system. The diameter of the beam remains on the order of a few mm. The photograph of the ion gun is shown in figure 11.

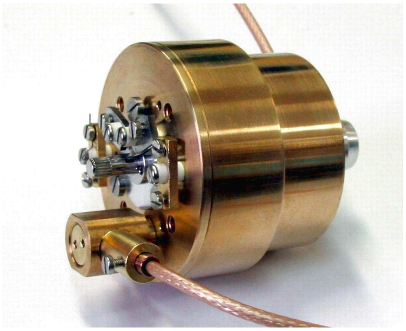

Figure 11: *The low energy ion gun itself [14]*

In the sample chamber of the Gentle Mill the pressure must be lower that $5*10^{-3}\ Pa$ as the hot tungsten ring from which the electrons are emitted is extremely sensitive to the partial pressure of H_2O and O_2. A higher pressure of these gases reduces the lifetime of the hot cathode. The average lifetime in well controlled conditions is 200-300 hours. Inside the gun, the pressure is higher than in the chamber due to the argon flow. With

increasing argon pressure (keeping the anode voltage constant) the ion current increases and upon reaching its maximum, decreases. This is shown in figure 13. Decreasing the anode voltage the optimum gas pressure also decreases.

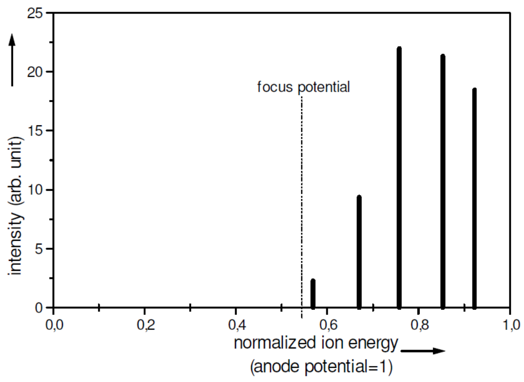

Figure 12: *Calculated ion beam energy distribution [14]*

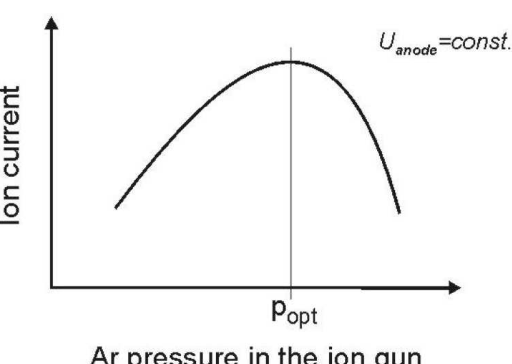

Figure 13: *Ion current as the function of the argon gas pressure [14]*

The ion current is measured on the sample holder and it contains more than one component as such: direct ion current from the ion gun and secondary electron current generated by the impact of ions in the aperture, sample and the sample holder. Tertiary electrons generated by the impact of secondary particles have to be taken into account as well and the list of contributors can be continued with decreasing importance (figure 14).

Unfortunately it is only possible to measure the total sample current without differentiating between the various contributions. To optimize the measured current, a few

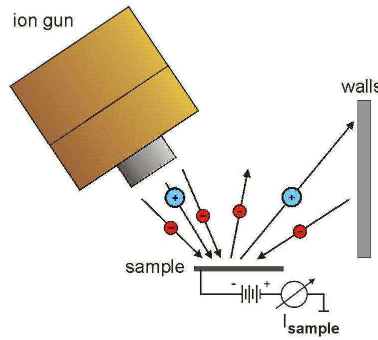

Figure 14: *Main components of the sample current [14]*

volts of negative bias $(5\ V - 10\ V)$ must be applied to the sample holder to prevent the low energy secondary electrons generated in the cathode from reaching the sample holder and decreasing the measured current. This has proven itself an efficient technique [14].

2.2.1 Simple Models of Ion Sputtering

Besides the accelerating voltage of the ion beam the most important quality which defines the properties of the ion sputtering is the angle of incidence. To reduce the radiation damage to the material glancing angles are preferable, but then the sputtering rate is very low (figure 15). Note that in this work the angle of incidence is always measured from the surface of the sample (figure 16). Therefore we have to find the optimum condition: not excessively damaging the sample, yet at the same time removing enough material.

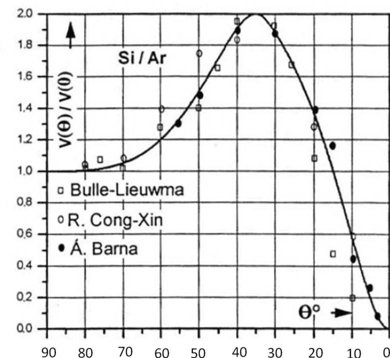

Figure 15: *Sputtering speed as the function of ion incidence angle (θ) measured by others on Si using Ar ion beam [15]. It is a very important curve as far as this work concerns. Though it was measured on Si the characteristics is similar in the case of our samples too.*

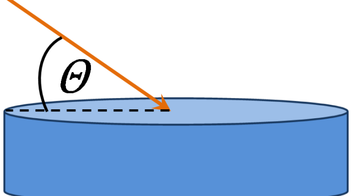

Figure 16: *Angle of incidence (θ) in this work is always measured from the surface of the sample*

A. Barna et al. gave simple but effective geometrical model for ion sputtering [16], which is presented here.

An important observation has to be stated first: surface roughening by ion beam is a macroscopic process, thus geometrical treatment is sufficient. Only singularities of the

topography, such as sharp edges and peaks cannot be treated this way, but sharp edges and peaks do not develop during ion sputtering [15].

At a time t_1 (figure 17) we have a surface with basic topological elements: inclined macrosteps. It is important that the size of a step is larger than the cascade induced by the ion beam. The steps are characterized by their inclination angle (α) measured from the average surface plane (figure 17). When the sample is homogeneous, the ion sputtering can only change the shape and the position of these steps. Their height can be changed only by their collision, this is the only way how they can disappear. Just as no step can disappear by itself, no step can appear during ion milling. If the sample is homogeneous, one can expect intensive surface changes if the lateral displacement of the steps (S_m) is large compared to the erosion speed $(V(\theta))$ (figure 17).

In figure 17 the initial surface at time t_1 is shown, along with the surface after a duration of milling, at time t_2. Points A, B and P are converted to A', B' and P' points. The lateral displacement can thus be written in the form:

$$S_m = V(\theta)\frac{\frac{V(\alpha)}{V(\theta)\cos\alpha} - 1}{\tan\alpha}.$$

$V(\theta)$ and $V(\alpha)$ are erosion speeds measured in the directions normal to the average surface and the inclined steps, respectively.

S_m depends strongly on $V(\theta)$, on the material and on the sputtering conditions. Its value can vary widely, it can be negative, positive or zero.

The conclusions of this model, which is valid in general for all homogeneous materials, are the following:

- S_m, the lateral step displacement speed is low when the angle of incidence, θ, is $10° < \theta < 30°$. Basically, no collision of steps takes place and the optimal angle can therefore be found in this range, where the topography of the surface is just slightly changed.

- However, when the angle of incidence is smaller than $5°$, S_m can be many times larger than $V(\theta)$, which results in rapid movement of the steps and therefore annihilation for rotated samples. In this range the sample surface can be polished smoothly, but looking at the sputtering rate curve above (figure15), one can ob-

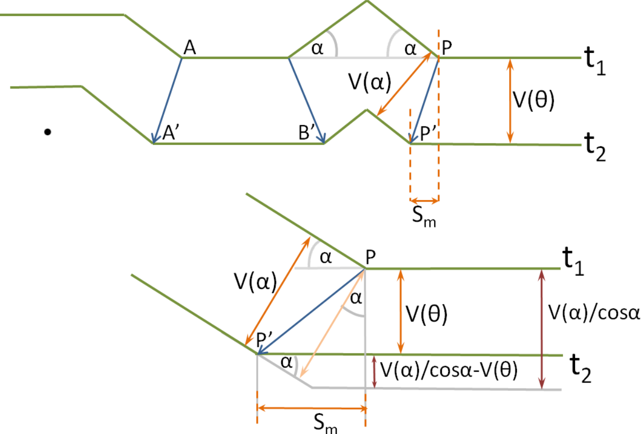

Figure 17: *Basic elements and considerations in the model of sputtering (own figure based on [16])*

serve that the speed decreases rapidly. If there is a certain thickness, which must be removed to yield a smooth surface, it will cost time.

- In the above mentioned $\theta < 5°$ range the ratio of lateral displacement speed to the erosion speed ($\frac{S_m}{V(\theta)}$) is large and depends only slightly on α if $\alpha > 90° - \theta$, which means that more all less the annihilation is equally effective for every step for rotated samples.

All the discussion above is true for homogeneous materials, but only a few materials (like amorphous materials) are like that. The materials discussed in this work are not homogeneous, rather polycrystalline. The model provides a good starting point, but will need a bit of change.

Let this change be that in the homogeneous matrix, there are inhomogeneities in domains near to the surface with a sputtering rate higher or lower than the sputtering rate of the matrix. In a material like this hillocks and dents appear during ion sputtering. This is the main difference between inhomogeneous and homogeneous materials. For the latter, as was mentioned above, no steps appear or disappear during ion sputtering. In the case of the inhomogeneous material steps appear when sputtering the domain with different sputtering rate.

Two basic cases can be distinguished: whether the steps that appear can be or cannot be displaced. Figure 18a shows the case where the steps remain where they appeared,

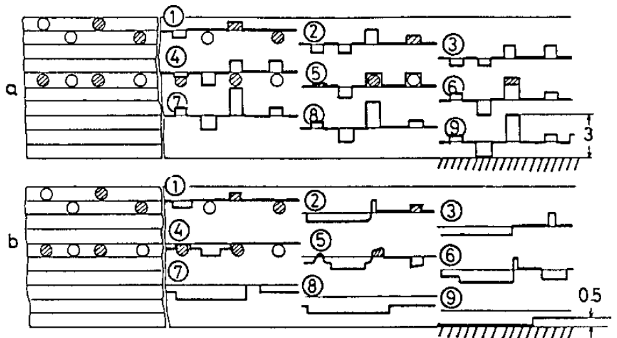

Figure 18: *Homogeneous matrix containing inhomogeneities with lower and higher sputtering rate [16]*

whereas in figure 18b the steps can be displaced and the lateral displacement (S_m) is half of the sputtering speed of the matrix. On the left hand side of figure 18 the initial distribution of inhomogeneities is shown. The full circles have a higher sputtering rate than the matrix and the empty circles have a lower. On the right hand side the state of the surface is showed after layers with equal thickness are removed. The thickness of the removed layer equals with the thickness of the inhomogeneity. Hillocks and dents are formed and their heights change until the inhomogeneity is completely removed. When lateral displacement is allowed (figure 18b) in the positive direction the heights of the hillocks decrease and the depth of the dents increase. If steps can move in the negative direction hillocks grow, dents get more shallow. We can conclude that until homogeneous materials are smoothed during ion sputtering, a homogeneous matrix with inhomogeneities roughens at first and then begins smoothening.

The situation is somewhat different when a significant volume of inhomogeneities are contained by the homogeneous matrix statistically distributed. In this situation, many permanent hillocks and dents are produced during ion sputtering and they can move e.g. when the size of the dent increases due to step movement, the depth of the dent increases when a new inhomogeneity impinges on the former dent with increased size. We can distinguish three cases in the prospect of the lateral displacement speed:

- With low lateral displacement speed and low density of inhomogeneity, the probability for the dents to deepen is low, because dents and inhomogeneities do not encounter often.

- With a higher lateral displacement speed, the probability of dents and inhomogeneities encountering is increased, but the maximum depth which a dent can reach is limited.
- At very high lateral displacement speed, microsteps vanish quickly from the surface and the topography will not be changed by further sputtering.

The importance of this simple model for this work is that it is able to describe the behaviour of polycrystalline material during ion milling. Different orientations has different sputtering rate.

While in both SEM and in FIB the sample is moved to the area of interest before the milling starts, there is no movement of the sample after that. In the case of Gentle Mill the beam is not focused on a specified point or area of the sample, instead the whole surface is sputtered. Therefore there is no need for sophisticated sample movements in Gentle Mill. Only the angle of incidence can be adjusted and in order to avoid or reduce the artifacts of ion sputtering the sample can be rotated or oscillated during sputtering. In table 2nd the basic properties of the beams used are summarized.

	SEM	FIB	GM
Particle	electron	Ga	Ar
Energy (keV)	1 - 30	2 - 30	0.1 - 2
Beam movement	scanning	scanning	static
Sample movement	static	static	static/**rotating**/oscillating
Focusing	strong	strong	slight
Beam diameter	nm	nm	mm

Table 2: *Properties of the different beams used for preparation and investigation*

2.3 Electron Backscatter Diffraction

2.3.1 Theory of EBSD

To understand the information provided by EBSD investigation, one has to understand the physical process that leads to the formation of the Kikuchi patters. The aim of this chapter is to describe this process.

Kikuchi patterns are observable not only in SEM, but in TEM as well. To be able to understand the basics, let us start from the simpler case of how Kikuchi patterns are formed in TEM.

As a reminder, in TEM, high energy (a few hundred keV) electrons penetrate through a very thin sample $(100\ nm)$. To see the diffraction of the electrons, the detection is positioned into the focal plane of the objective lens.

In the first step, let us consider only the kinematic model of electron scattering: consider only single, elastic scattering from the crystal planes and neglect the multiple and inelastic processes. This will lead us to Bragg's law:

$$n\lambda = 2d_{hkl} \sin\theta,$$

where n is the order of the reflection, in most cases equal to 1, λ is the wavelength of the radiation used, θ is the angle of incidence and d_{hkl} is the distance between the crystal planes.

Despite its simplicity, it is the most useful equation in diffraction. It was first proposed by William Lawrence Bragg and his father and supervisor, Sir William Henry Bragg in 1913 to explain the curious patterns or spots observed when X-ray are reflected from crystalline material [18]. As W. L. Bragg himself explained, the crystal is modelled by parallel planes separated by constant distance: d_{hkl}. Radiation with the wavelength λ will produce a Bragg peak, or in our case a bright line, if the interference of their reflection from different planes is constructive, which will occur if their phase shift equals $n2\pi$. (See figure 19.)

W. L. Bragg and Sir W. H. Bragg won the Nobel Prize in physics in 1915 "For their services in the analysis of crystal structure by means of X-rays". W. L. Bragg is the youngest ever Nobel laureate, being awarded the prize at the age of 25.

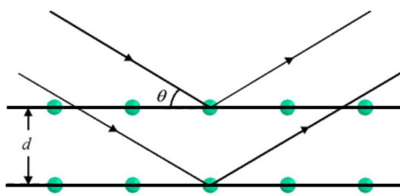

Figure 19: *Bragg's law*

There is another, very different approach to the problem of electrons (or X-rays, or neutrons) scattering in crystalline material, which leads to the same conclusion. This approach was suggested by Max von Laue, who was awarded the Nobel Prize one year prior to the two Braggs, in 1914, "for his discovery of the diffraction of X-rays by crystals". In his approach, the incident wave was scattered by individual atoms instead of crystal planes.

The origin of a given unit cell in the structure is given by the vector $\boldsymbol{r_{cell}}$:

$$\boldsymbol{r_{cell}} = m\boldsymbol{a_1} + n\boldsymbol{a_2} + o\boldsymbol{a_3},$$

where $\boldsymbol{a_1}$, $\boldsymbol{a_2}$, $\boldsymbol{a_3}$ are non-coplanar vectors defining the coordinate system.

Each unit cell contains $p \geq 1$ atoms at positions given by the vectors $\boldsymbol{r_{atom}}$.

The incident electron beam is a plane wave with wave vector $\boldsymbol{k_0}$ and wavelength λ and each atom scatters the wave elastically through an angle θ with an amplitude $f(\theta)$. The wave vector of the scattered wave is noted by $\boldsymbol{k}$.

$$\boldsymbol{k_0} = \frac{1}{\lambda}\boldsymbol{n_0}, \qquad \boldsymbol{k} = \frac{1}{\lambda}\boldsymbol{n}, \qquad |\boldsymbol{n}| = |\boldsymbol{n_0}| = 1.$$

The path difference between waves scattered by two atoms separated by $\boldsymbol{r}$ (figure 20):

$$\Delta = \boldsymbol{nr} - \boldsymbol{n_0 r},$$

then the phase difference is:

$$\Phi = \frac{2\pi}{\lambda}\Delta = 2\pi(\boldsymbol{k} - \boldsymbol{k_0})\boldsymbol{r}.$$

Taking into account waves scattered by all atoms:

$$\Psi = \Psi_0 \sum_{m=0}^{N_1} \sum_{n=0}^{N_2} \sum_{o=0}^{N_3} \sum_{j=0}^{p} f_j(\theta) e^{2\pi i (\boldsymbol{k}-\boldsymbol{k_0})(\boldsymbol{r_{cell}}+\boldsymbol{r_{atom}})}.$$

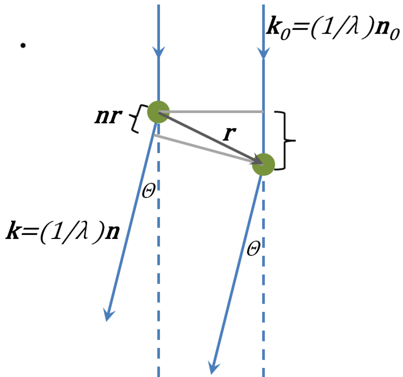

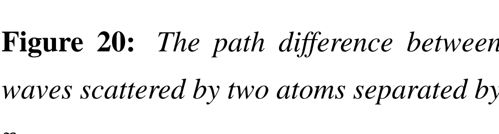

Figure 20: *The path difference between waves scattered by two atoms separated by* $\boldsymbol{r}$

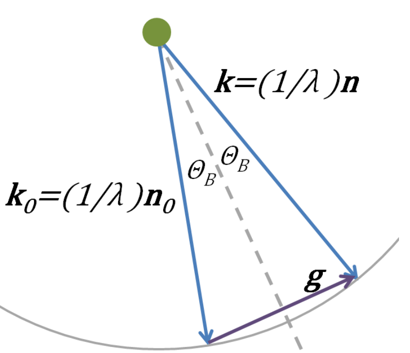

Figure 21: *The Ewald sphere defined by* $\boldsymbol{k_0}$ *showing that Laue and Bragg conditions imply the same criteria for diffraction*

N_1, N_2, N_2 are the numbers of the unit cells at each directions, Ψ_0 is the amplitude of the incoming wave, which can be considered equal to unity and $f_j(\theta)$ is the scattering amplitude of the jth atom in the unit cell.

We can separate this equation into the well known structure factor (S) and form factor (F):

$$\Psi = \sum_{j=0}^{p} f_j(\theta) e^{2\pi i(\boldsymbol{k}-\boldsymbol{k_0})\boldsymbol{r_{atom}}} \times \sum_{m=0}^{N_1} \sum_{n=0}^{N_2} \sum_{o=0}^{N_3} e^{2\pi i(\boldsymbol{k}-\boldsymbol{k_0})\boldsymbol{r_{cell}}} = S \times F.$$

The interference is constructive if the argument of the term $e^{2\pi i(\boldsymbol{k}-\boldsymbol{k_0})\boldsymbol{r_{cell}}}$ equals integer times 2π for every unit cell. This criteria yields the Laue condition of diffraction:

$$(\boldsymbol{k} - \boldsymbol{k_0})\boldsymbol{a_i} = h_i.$$

So $(\boldsymbol{k} - \boldsymbol{k_0})$ has to equal a reciprocal vector:

$$\boldsymbol{k} - \boldsymbol{k_0} = \boldsymbol{g} = h\boldsymbol{b_1} + k\boldsymbol{b_2} + l\boldsymbol{b_3},$$

where $\boldsymbol{b_i}$ defines the reciprocal coordinate system:

$$\boldsymbol{b_i} = \frac{\boldsymbol{a_j} \times \boldsymbol{a_k}}{\boldsymbol{a_i}(\boldsymbol{a_j} \times \boldsymbol{a_k})}.$$

Each reciprocal vector perpendicular to a set of parallel crystal planes with the Miller indices (hkl) has a length corresponding to the distance between the planes, $d_{hkl} = \frac{1}{|g|}$. It is easy to see in figure 21 that the Laue condition of diffraction is exactly the same as the Bragg condition [19].

d_{hkl} can be computed easily from the lattice parameter a for cubic materials (Cu, Al and Ag described in this work, are cubic, fcc materials):

$$d = \frac{a}{\sqrt{h^2 + k^2 + l^2}}.$$

We can now write Bragg's law in the following form:

$$\frac{\lambda}{2a} = \frac{\sin\theta}{\sqrt{h^2 + k^2 + l^2}}.$$

If we fix the wavelength of the electron beam, as we can do in SEM by adjusting the accelerating voltage, Bragg's law gives us a simple relation between the angle of incidence and a set of Miller indices of a crystal plane. We can measure the angle θ of the bright spot or line on the screen and thus tell the Miller indices of the related plane.

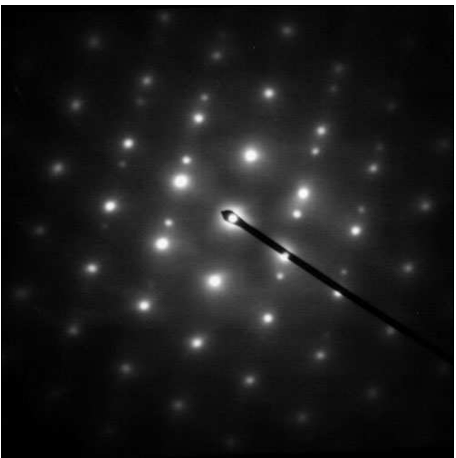

Figure 22: *TEM diffraction pattern from a twinned grain of fcc austenitic steel (source: Wikipedia)*

These pictures are valid as long as the sample is thin enough, so the path of the electrons is too short for multiple scattering. The planes at the bottom of the sample

experience the same intensity as the planes on the top. The typical TEM sample has a thickness where this condition is obeyed. Single, elastic scatterings on a single crystal sample of the monoenergetic electron beam leads to the usual TEM diffraction pattern with well defined spots (figure 22).

If we increase the thickness of the TEM sample we exit the range where kinematic model of scattering is valid. Due to the increased probability of multiple scatterings, the beam that reaches the crystal planes inside the sample is no longer parallel, but rather diffuse. The electrons arrive to the crystal planes from all directions. This means that there are electrons arriving at the Bragg angle (θ_B) for each set of crystal planes. The locus of the reflected electrons is the surface of a cone, called Kossel cone. Every bright Kossel cone has a dark mirror image pair. This dark cone represents the directions from which the electrons are missing (figure 23). Of course, due to the multiple scatterings there are electrons arriving to the other side of the plane under the Bragg angle (θ_B), and they are scattered in the directions, where the electrons from the direct beam are missing but the probability of this process is much lower. As a result, we see bright and dark, parallel lines in TEM (figure 25).

The axis of the Kossel cones are the normal of the plane where the electrons are reflected from and its half apex is $(90° - \theta_B)$. (figure 24), and the angular spacing of the Kikuchi lines is $2\theta_B$.

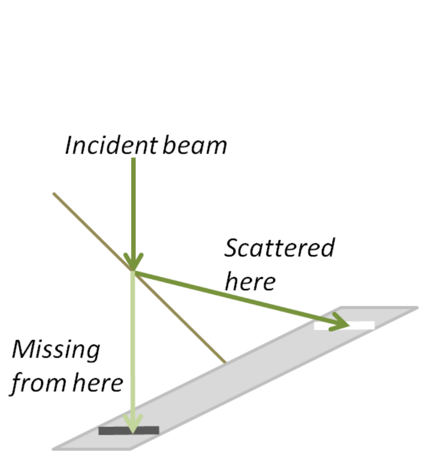

Figure 23: *The formation of bright and dark Kikuchi lines in TEM*

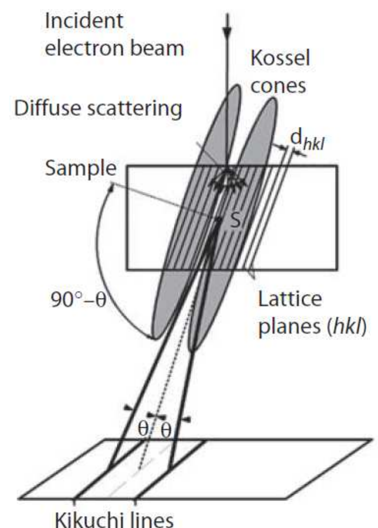

Figure 24: *Formation of Kossel cones in the TEM [1]*

Taking the typical electron wavelength and the typical interplanar spacing, the Bragg angle can be estimated to be under 1°, meaning that the cones are almost flat. Therefore, the intersections of the cones with the flat detector will be lines. Indeed, we experimentally observe parallel lines, the so called Kikuchi lines.

Now that the formation of the Kikuchi lines in transmission electron microscope is understood, we can turn to what happens in the scanning electron microscope.

As a reminder, in SEM a highly focused (nm diameter) electron beam scans the surface generating various products, among them backscattered electrons. Backscattered electrons are diffusely reflected from the original incident beam, preserving most of their energy. On their way out of the sample they are scattered by the crystal planes, leading to diffraction. As a consequence, it can be imagined that in case of EBSD the effective electron source is inside the sample, radiating in every direction.

In the case of usual SEM imaging, where the beam is normal to the surface of the specimen, the backscattered electron yield is very poor, insufficient to observe diffraction. If we increase the angle between the surface normal and the electron beam, the backscattered electron yield dramatically increases (figure 26).

In figure 27, the formation of Kossel cones in the bulk sample using SEM is shown. The picture is very similar to the one explained for the case of TEM, one difference being is that the effective diffuse electron source is now inside the sample. The other very important difference is, that the electrons propagating out from the sample have no specified direction, so the scattering on the two sides of the planes had equal probability.

Figure 25: *Picture taken on Kikuchi lines using TEM [1]*

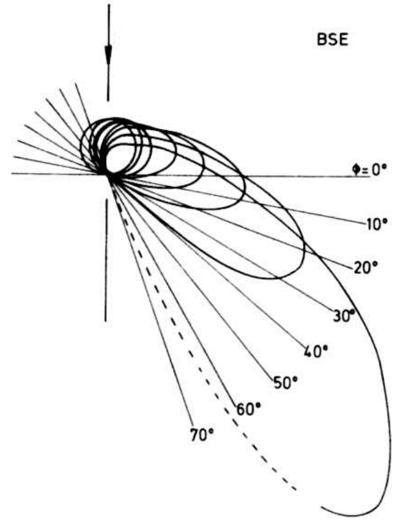

Figure 26: *Backscattered electron yield increases with increasing angle of incidence [19]*

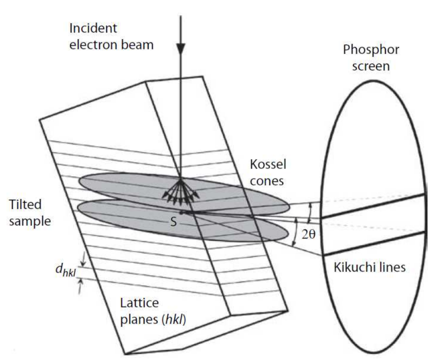

Figure 27: *Formation of Kossel cones in the SEM [1]*

Therefore, in this case we expect to see only bright parallel lines.

In figure 28 Kikuchi pattern obtained on Ni using SEM is shown. If we look closely enough, we can realize that something does not fit to the model described above: the lines are not bright, but dark and between two dark lines there is a bright band. The intensities observed on the Kikuchi pattern are the exact opposite that we would expect from Bragg's law. In other words the kinematic model of scattering is no longer valid and we must take into account multiple scattering and inelastic contributions. This is the dynamic model of scattering. In the dynamic theory, the Schrödinger equation has to be solved for the following problem: if a plane incident wave satisfies the boundary conditions at the interface crystal-vacuum, how will it be transformed into a wave-field $\Psi(r)$ having the same periodicity as the crystal?

The Schrödinger equation for the electron in the crystal is the following:

$$H\Psi = (-\frac{\hbar^2}{2m}\nabla + V(r))\Psi(r) = E\Psi(r)$$

where $V(r)$ is the periodic crystal potential. Since it is periodic, it can be Fourier expanded with the reciprocal lattice vectors. Making use of the Fourier decomposition we get the following equation:

$$\nabla^2\Psi + \frac{2m}{\hbar^2}(E - \sum_h V_h e^{2\pi \boldsymbol{hr}})\Psi = 0$$

The incident beam is still, of course, plane wave, but when it enters the crystal, due to the periodic potential, it has to be the superpositions of Bloch waves.

The equation can be solved inside the material, it gives n beams with silghtly different wave vectors. This is referred as to n-$beam$ case. Each wave vector has a different excitation point, which means that in the Ewald picture, we have n Ewald spheres with different origins and different radii. The intensity what we see in the diffraction pattern, is the interference of these n beams.

Analytically this problem cannot be solved, except the 2-beam case. Simulations showed that considering 3 beams, the intensity distribution in the EBSD's diffraction pattern is going to be the way we see it in experiments (figure 29) [19]: bright band with dark borders.

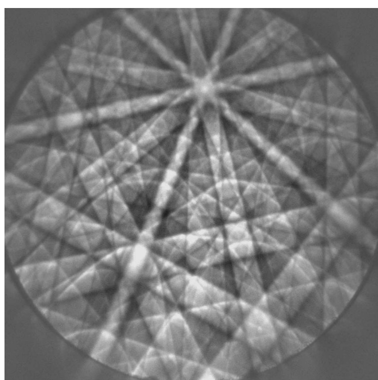

Figure 28: *Kikuchi pattern obtained on Ni using scanning electron microscope (our image)*

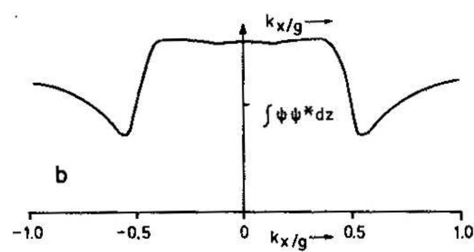

Figure 29: *The calculated intensity of a band on the EBSD diffraction pattern [19]*

2.3.2 Instrumentation of EBSD and Data Processing

The instrumentation of EBSD became quite simple since it can be part of a scanning electron microscope. SEM provides a highly focused electron beam that scans the chosen area of the surface. As was mentioned in the previous section, the sample needs to be tilted to optimize backscattered electron yield. Electrons scattered from the crystalline sample produce a diffraction pattern which is detected by a phosphorous screen

placed right in front of the sample (figure 30). At the phosphorous screen the electrons are converted to photons and the pattern is recorded by a high speed CCD camera before being indexed by the computer (400 pattern can be indexed per second). A schematic diagram of the instrumentation is shown in figure 30 and a photograph of the setup as it is in the chamber is shown in figure 31. The sample is tilted to 70° and the camera is tilted with an extra 7° with respect to the horizontal. In figure 31 the path of the electrons is shown with red arrows.

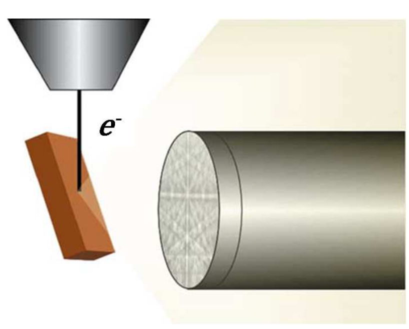

Figure 30: *Schematic diagram of EBSD setup [20]*

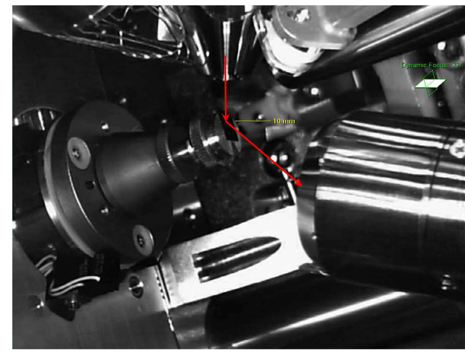

Figure 31: *EBSD setup as it is*

The collection of the data is relatively simple, but the processing, on the other hand, is quite difficult. Probably the biggest challenge is the computer identification of the bands. Due to inelastic effects and multiple scattering, the signal-noise ratio of the EBSD patterns is very small. To improve this, the first step is always the background subtraction, which one can perform by integrating the diffraction patterns from a larger area of the polycrystalline sample. This results in an image avareged from all grains in the field of view which is then subtracted by the computer from the actual diffraction pattern. After the subtraction process, the bands are recognizable to the human eye, but for the computer it is not so trivial. The bands are not bright enough, often not continuous and intersect with each other.

After many good, but failed approaches, Krieger Lassen [21] and Kunze [22] proposed the usage of the Hough transformation, which had already been used in use for similar problems. By this procedure lines are transformed into points, which are much easier to detect by computers.

Initially we have a picture in an (x, y) coordinate system with (x_i, y_i) points. This

picture is transformed into the so called Hough space with coordinates ρ and θ according to this relation:

$$\rho = x_i \cos\theta + y_i \sin\theta, \qquad \theta \in (0^\circ, 180^\circ), \qquad \rho \in (-R, R).$$

This relation maps each coordinate (x_i, y_i) on a straight line in the Hough space with coordinates (ρ, θ). In the real space we put the origin of the (x, y) coordinate system in the middle of the picture. Each line in the picture can be characterized with two values: ρ is the distance between the line and the origin, θ is the angle between the line's normal and the x axis. The principle is illustrated in figure 32.

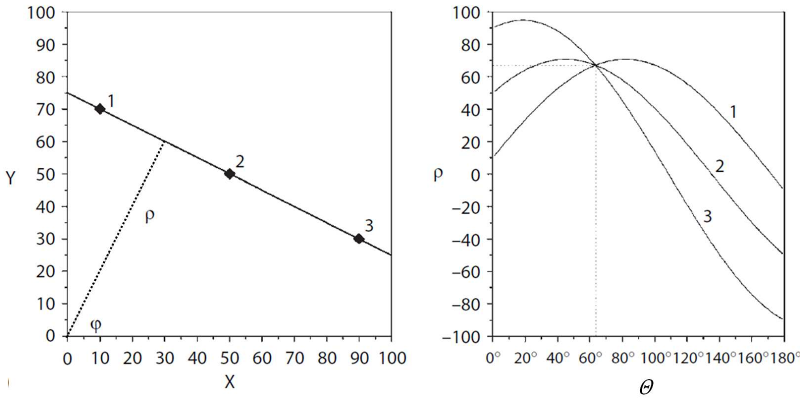

Figure 32: *Principle of Hough transformation [1]*

Each individual point in (x, y) space corresponds to sinusoidal curve in Hough space, since one point can define an infinite number of lines, but their ρ and θ coordinates are not independent. Having two or more collinear points in (x, y) space, their curves intersection in Hough space will give the point (ρ, θ) corresponding to the line connecting the points. This is what is shown in figure 32.

A special type of Hough transformation, known as the gray-tone weighted Hough transform, or Radon transformation [23] is used when processing EBSD patterns. In the case of EBSD patterns each point in the (x, y) space has an intensity, $I(x, y)$. All intensities lying along the lines are summed up, giving the total intensity, $I(\rho, \theta)$ in Hough space. A special case of the Radon transformation is shown on figure 33. On the original (x, y) picture the area where the transformation takes place ($\rho \in (-R, R)$) lies

inside the circle. Two lines with finite width are shown on a constant grey background. Clearly this is an ideal scenario, because in a real diffraction pattern the background is always noisy.

On the Hough transformed picture, the two lines are transferred into two spots with finite diameter. A characteristic butterfly shape can be observed around each spot due to the fact that the lines are built up of each individual points and that the Hough transform of each individual point is a sinusoidal curve, as was mentioned above. At the spots, the curves intersect and their intensities are summed.

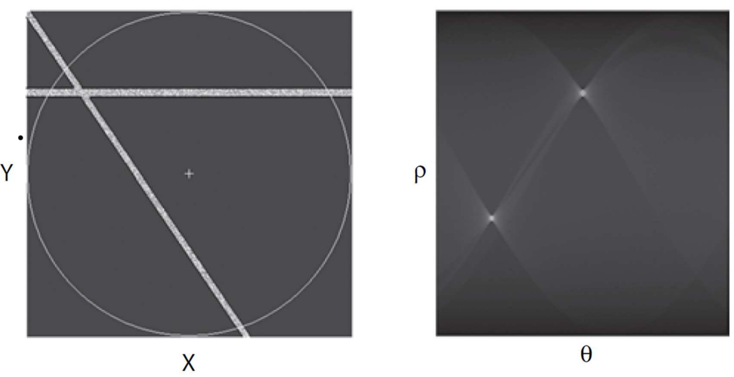

Figure 33: *Special case of Radon transformation [1]*

After the Hough transformation, the next task is to find the brightest peaks. For this, a filter called a butterfly filter searches for the characteristic butterfly shapes, which will help in finding the peaks. The outputs are the Hough parameters of the peaks which define the middle line of the brightest bands. In figures 34 and 35 a diffraction pattern obtained on silver and its Hough transformed image is shown.

After finding the bands, they are sorted by their intensities and the indexing can take place to determine the orientation of the crystal producing the pattern.

EBSD requires all information on the material we are about to investigate. The orientation of the crystallites found on the surface is the only output of the EBSD measurement. To determine this, we have to know not only the elements contained in the sample, but also the crystal structure they form. There is a possibility to simultaneously collect X-ray photons produced during an EBSD measurement, thus, map out the distribution of the elements on the sample surface. Useful examples will be shown later. If we have no information on the crystal structure, the experienced eye can tell the crystal

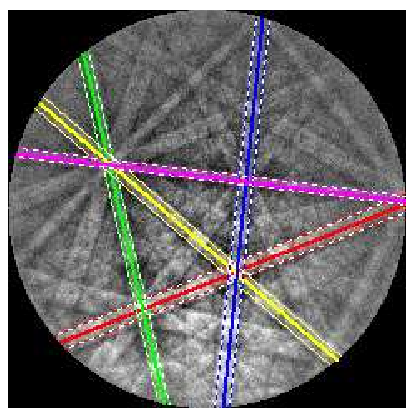

Figure 34: *Diffraction pattern obtained on a silver sample (our image)*

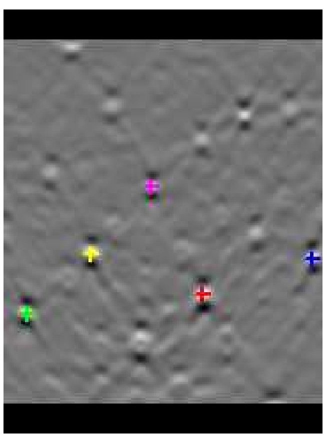

Figure 35: *Hough transformed of the diffraction pattern (our figure)*

system, by checking a few diffraction patterns. Thus, by combining the compositional analysis with an experienced user, we can get information on the material itself, but in general it is expected as input, not output.

The first step in orientation determination, after defining the material and its crystal structure, is the generation of a lookup table from the interplanar angles of the reflecting planes. Then a list is constructed considering all possible set of three bands reflected by these planes and their symmetric equivalents. The next step is forming band triplets from the detected bands on the measured diffraction pattern.

Now we have a list of calculated band triplets and measured band triplets, we can start comparing them. In most cases, more than one set of calculated triplets (i. e. solution) fits any measured triplet. To determine the most probable one, a voting scheme is followed. An example for the voting procedure is shown in figure 36.

In figure 36, the experimentally found band triplets are listed in the first column. Each colour corresponds to a different band. In the top row, the possible solutions are listed. Each solution gets a vote if the detected band triplet is included in it, these are noted with X. The most probable solution is the one receiving the most votes, here solution number 3.

The voting procedure provides the possibility to measure the confidence of the indexing. The value describing this is called 'confidence index' and calculated as follows:

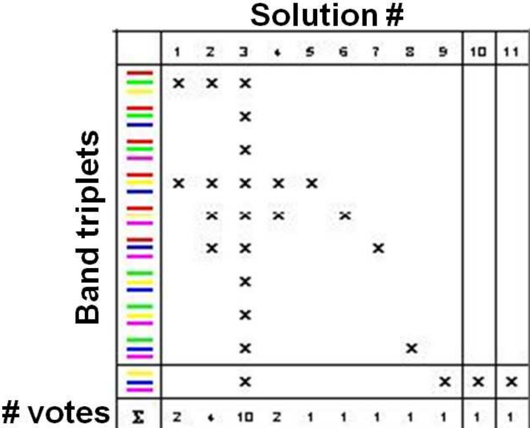

Figure 36: *Voting table to determine the most probable orientation [24]*

$$CI = \frac{V_1 - V_2}{V_{ideal}},$$

where V_1, V_2 are the number of votes that the best and the second best solution received, V_{ideal} is the number of all possible triplets that can be formed with the detected bands.

The confidence index ranges from 0 to 1. According to figure 36:

$$V_1 = 10, \qquad V_2 = 4, \qquad V_{ideal} = 10,$$

$$CI = \frac{10 - 4}{10} = 0.6.$$

Experiments have showed that fcc materials with a CI higher that 0.1 were correctly indexed 95% of the time [24].

There is also a parameter which measures the quality of the diffraction pattern. This is called image quality (IQ).

The image quality equals the sum of the detected peak intensities in Hough space. The blurrier or vaguer the band, the less definite the peak and the smaller the intensity. No upper limit can be determined for this value. Since we get an image quality from every point, we can map it just like an SEM image: pixels with brightness according to the IQ at the point. In figure 37, an image quality map is shown and next to it, in figure 38, the SEM image of the area were the IQ map was obtained. Observe that the holes and

scratches on the surface (figure 38) appear in the IQ map (figure 37) too. The boundaries of the grains are dark because the diffraction volume may contain both crystal lattices separated by the boundary, and thus, the diffraction pattern will be composed of a mix of both patterns, leading to a lower quality pattern [24]. It is very important that the intensities of the IQ maps cannot be compared ever. It is composed as the highest IQ parameter corresponds to the white colour and the lowest to the black. It only shows the differences of the actual measurement.

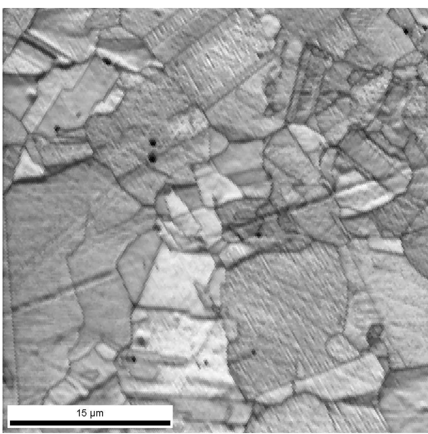

Figure 37: *Image quality map obtained on copper (our image)*

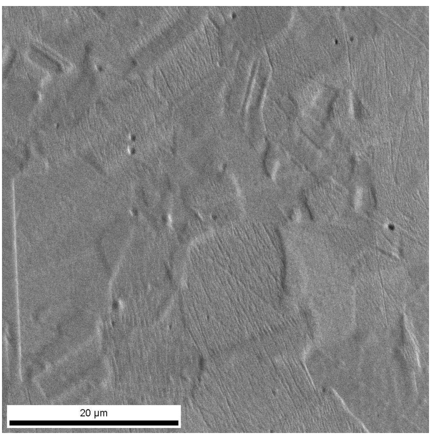

Figure 38: *SEM image of the area where the image quality map (in figure 37) was measured (our image)*

The relation of the image quality to the diffraction pattern is very simple: just the sum of intensities. On the other hand, the relation of the image quality to the material itself is more difficult. We used the IQ parameter to qualify the surface of the material, but since it depends on many factors, we had to be careful. A list of the most important factors that can have an effect on the image quality and the precautionary measures to eliminate them are described below.

- The intensity of each band depends on the number of electrons producing it, therefore, image quality depends on everything that can alter the backscattered electron yield: accelerating voltage, electron current, average atomic number in the volume investigated and deviations from the $70°$ tilt. We can fix the accelerating voltage $(20\ kV)$ and the sample current $(4\ nA)$. The dependence on the atomic number means that IQ parameters obtained from different compositions can not

be compared. Deviations from the 70° can be caused by surface topography or by incorrect sample mounting. The latter can be prevented by careful preparation. The surface topography is, in fact, the focus of this work.

- IQ depends on the orientation of the crystal, but the relation is not straightforward. Some bands have higher structure factor than others, thus, some bands are brighter than others and in a diffraction pattern the bands are not equally presented. When the orientation changes their length changes and so the IQ can be slightly different for two orientations with the same visible quality. The image qualities presented in this work are averaged over the measured area. In this area, many grains with different orientations are presented. By averaging, this deviation can be minimized, but it sill remains a random error.

- IQ also depends on the conditions of the measurement (contrast, brightness, etc.). The same parameters must be used for each sample to be able to compare the image qualities.

- Strain in the material makes the bands blurry. Indeed, it is possible to use IQ to give qualitative description of the strain distribution in a microstructure [25]. We were using as similar samples as possible to reduce the deviations in the IQ due to strain.

- The most important contribution to IQ, however, the quality of the surface. The less perfect the crystal, the lower the image quality.

In other words, keeping all possible conditions constant during the measurements, the image quality will give us information on quality of the surface.

At the end of the data collection and indexing process, the information is displayed as a picture, with different colours according to the orientation (figure 39).

The orientation contains 3 dimensions of information which have to be displayed in 2D. There are many ways of representing 3D texture data in 2D, we shall use the so called inverse pole figure and it will be detailed here.

First, the stereographic projection has to be understood. (See figure 40.) With the stereographic projection 3D angular relations can be displayed in 2D, such as angles between crystal planes.

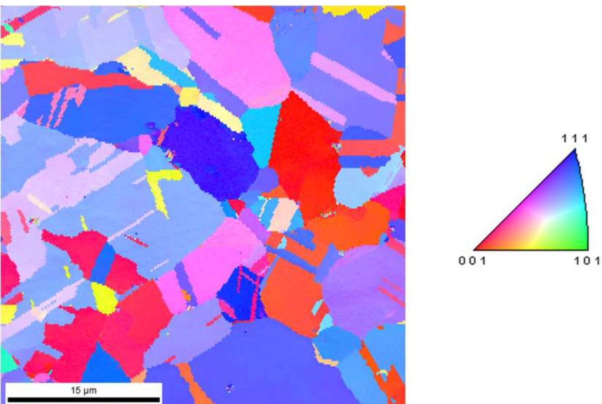

Figure 39: *Orientation map obtained on a copper surface and the inverse pole figure (our image)*

The crystal can be represented as a set of vectors normal to the crystal planes. The angular relations between the normals and the planes are the same. Stereographic projection starts with a spherical projection, which means that the origin of the crystal is placed at the origin of a sphere and the normal vectors of the planes intersect with the sphere resulting in a pole for each plane. The symmetry of the crystal is projected onto the sphere as well.

After the spherical projection, using geographical terminology, each pole on the Northern Hemisphere is projected from the South Pole (S) onto the equatorial plane. Typically, the poles from the Northern Hemisphere are denoted by full circles and the poles from the Southern Hemisphere denoted by empty circles. The angular relation-

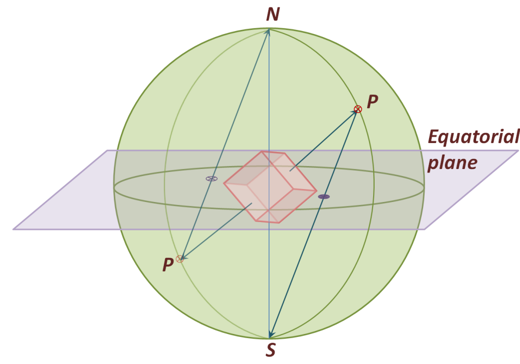

Figure 40: *Stereographical projection*

ships between the normals are preserved during the stereographic projection.

In figure 41, the [100] stereographic projection of a cubic crystal is shown. The z axis is chosen to be parallel to [100] direction, so (100) plane is first projected to the North Pole, then to the middle of the circle. In the figure, only the poles from the Northern Hemisphere are shown, but we still get the full set of planes in the crystal, because the equatorial plane is a mirror plane. Thus, the poles from the Southern Hemisphere would be projected onto their northern mirror image pairs.

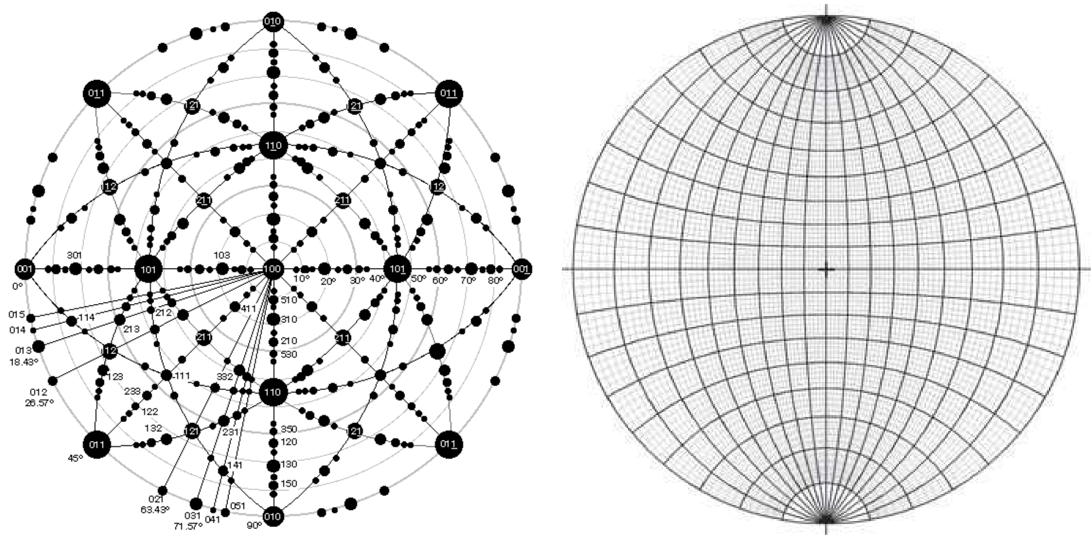

Figure 41: *The [100] stereographic projection [26]*

Figure 42: *Wulff net for measuring angles in stereographic projection; thick lines - 10°, thin lines - 2° [1]*

As mentioned previously, the symmetries and angular relations between the planes are preserved in the stereographic projection. To help reading the angles between the poles, a so called Wulff net is used which is a grid marked in 2° intervals (figure 42).

Due to the preserved symmetries, the stereographic projection can be divided into unit triangles, from which the whole projection can be built. The higher the symmetry, the smaller the unit triangle. In figure 43, the unit triangles for different crystal systems are shown. In the cubic system, there are 48 unit triangles in the projection (figure 43a) if both hemispheres are considered [1].

In a pole figure the coordinate system of the projection is fixed to the sample, such as, for example the normal of the sample is directed to the direction of the z axis. In the inverse pole figures, just the opposite is made, the coordinate system of the projection is

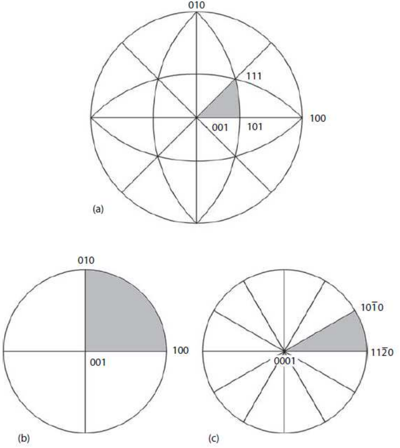

Figure 43: *Unit triangles in stereographic projection for (a) cubic, (b) orthoromic and (c) hexagonal systems [1]*

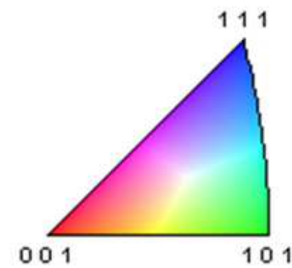

Figure 44: *Inverse pole figure for the cubic system*

fixed to the single crystal (as in figure 41), and the distribution of the sample normal is projected on the pole figure. Usually the stereographic projection is reduced to a single unit triangle as it can be seen in figure 44.

3 Measurements

We performed the same series of measurements on copper, aluminum and silver samples. The copper and aluminum samples had a cylindrical shape and the silver samples were thin triangles. Parameters of the different specimens are summarized in table 3. All samples were mechanically polished in the laboratory of Technoorg-Linda Ltd. Co. The steps of mechanical polishment were as follows:

1. Grinding paper 500-grit (35 μm)
2. Grinding paper 2000-grit (8 μm)
3. Diamond paste 7 μm
4. Diamond paste 2 μm

	Atomic number	Atomic mass (amu)	Bravais lattice	Lattice parameter (nm)	Thickness (mm)	Diameter (mm)
Cu	29	63.546	fcc	0.361	1.2	3
Al	13	26.982	fcc	0.405	1.3	2.5
Ag	47	107.87	fcc	0.409	0.4	5

Table 3: *Parameters of the samples*

The aim was to probe the Gentle Mill's and FIB's capabilities in preparing surfaces for EBSD investigation, compare the results and finally to give effective and fast protocols for sample preparation.

As mentioned in the previous chapter, the average image quality of each map was used to measure the quality of the surface. As such, we kept each parameter fixed for the same material. These parameters are summarized in table 4. Image qualities obtained on specimens of the same material are comparable, but not in case of samples made of different materials.

The last two columns of table 4, gain and exposure, are the adjustment parameters of the Hikari camera. Exposure fixes the time the beam dwells at each point, measured in milliseconds and the gain is the amplification of the original signal.

	SEM parameters		EBSD parameters		
	Acceleration voltage (kV)	Electron current (nA)	Working distance (mm)	Gain	Exposure (ms)
Cu	20	4	13	16.99	22.01
Al	20	4	12	17.30	22.94
Ag	20	4	20	19	16.46

Table 4: *Parameters used during orientation mapping*

We performed three sets of measurements on each material:

- Milling a quadratic pattern onto the specimen surface with different ion currents using the FIB.
- Sputtering the surface at different incident angles using the Gentle Mill.
- Sputtering the surface for different time intervals using the Gentle Mill.

Below, the details and conclusions of these measurements are given.

As a first step, we performed EBSD mapping on the raw, only mechanically polished surfaces. Note that the aim of the mechanical polishment was not to prepare a high

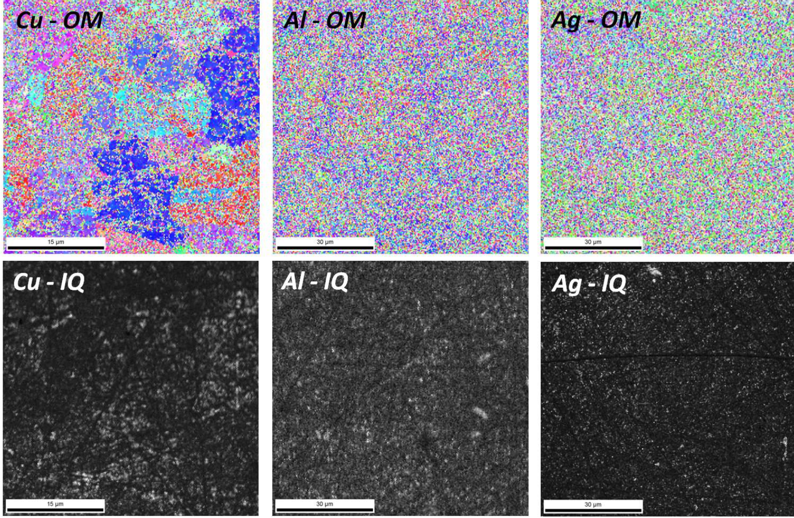

Figure 45: *Results of the mechanically polished samples*

quality surface, but to remove the rough bumpiness. In the images of the figure 45 it is indeed shown that the quality is not good at all. The IQ maps are almost all black and except for the copper, no grains are distinguishable.

3.1 Measurements Using Focused Ion Beam

When using FIB, both the accelerating voltage and the ion current can be adjusted. The higher the current, the more effective the sputtering and the less time is needed to mill the same geometry. On the other hand, as a drawback, we experienced that the quality of the milled surface decreased with increasing ion current. We wanted to see whether we could measure this decrease, whether we could observe the effect of the amorphous layer building up on the surface during high energy variable current ion milling and, finally, how low the current had to be to get a good surface for EBSD, if at all. The only parameter we changed was the ion current, the accelerating voltage was kept at $30\ kV$.

The samples were mounted on a tilted sample holder using conductive silver paint. The pretilt of the holder was $45°$. We required the initial tilt to be able to perform the FIB milling and the EBSD mapping with only stage movements.

In figure 46, the setup for the FIB milling is shown. The FIB column is at $52°$ from the vertical. By tilting the pretilted sample with $7°$, the surface is exactly parallel with the beam. We added an extra $1°$, this way the angle of incidence was $1°$ measured from the surface.

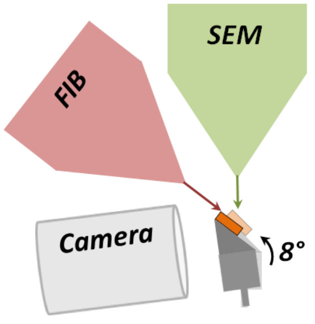

Figure 46: *Setup for FIB milling*

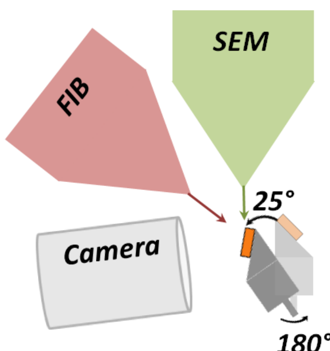

Figure 47: *Setup for EBSD orientation mapping*

In figure 47 the setup for EBSD is shown. The specimen tilt has to be $70°$. To ensure this the specimen had to be rotated by $180°$ and then an extra $25°$ tilt was added to the $45°$ pretilt.

Three identical trenches were cut into one sample of each material adjacent to each other using different currents (table 5). The geometry of the trench is shown in figure 48, the dimensions were $(x \times y \times z) = (20\ \mu m \times 5\ \mu m\ \times 20\ \mu m)$.

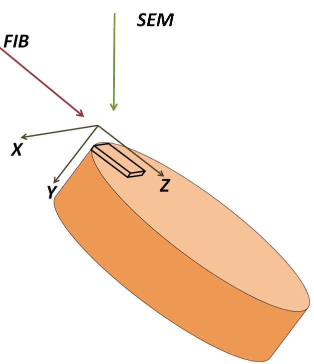

Figure 48: *The geometry of the trench milled on the surface of the sample using FIB*

To mill the trenches we used the in built pattern called Cleaning Cross Section (CCS). When CCS is used, the rectangle to mill is divided into lines. Instead of sputtering the whole area of the pattern, as is usually done, the pattern is sputtered line by line. The purpose of this procedure is to avoid, or rather reduce the redeposition onto the final surface.

Figure 49 was made using FIB for imaging. The cut shown with a red arrow and denoted $No.1$ is a finished trench, the yellow pattern shown with yellow arrow denoted $No.2$ is the pattern to be milled. The ion image were obtained on the copper sample. In figure 50 the three completed trenches are shown, with the ion currents specified.

As is shown in figure 50, the three currents used were: $15\ nA,\ 5\ nA$ and $3\ nA$. With

$x \times y \times z = 20\ \mu m \times 5\ \mu m\ \times 20\ \mu m$			
Current	15 nA	5 nA	3 nA
Time	15 min	45 min	90 min

Table 5: *Time of the sputtering for each ion current*

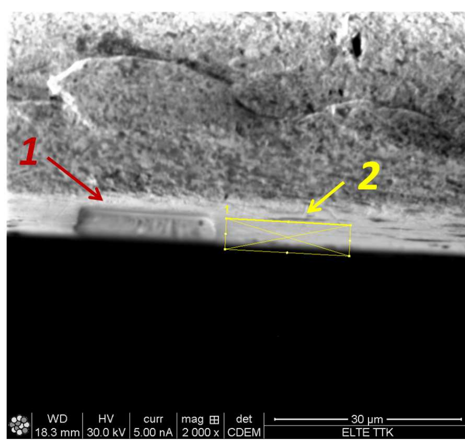

Figure 49: *Ion image on one ready trench (red) and on the pattern (yellow) - Cu sample*

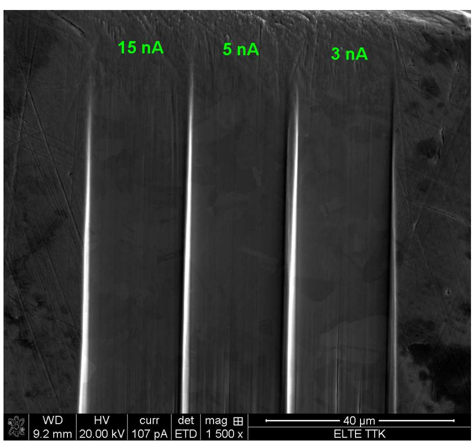

Figure 50: *Electron image on the three trenches specifying the ion current that was used to mill them - Cu sample*

decreasing ion current, the sputtering is less effective and thus, takes more time. In table 5, the times to mill the trench for each current are shown. The times were equal for each material.

After preparing the cuts with FIB, the sample was moved to the EBSD position shown in figure 47 and an orientation map was made on the whole area with all the three cuts included, to make them easily comparable. The results are shown in figure 51. The measurements on copper confirmed what was shown by Matteson et al. [12] that Cu does not amorphisize significantly under FIB. We cannot see any differences in the brightness of the three trenches on the image quality map. On the other hand, in the IQ maps obtained on aluminum and silver, the cuts prepared with $3\ nA$ seem much brighter than the other two. This could also confirm the suggestion that materials with larger lattice parameter amorphisize more willingly [12]. However, this would be a rapid conclusion, since not enough materials were investigated to establish a trend and the difference in the lattice parameter is only $0.04\ nm$.

Orientation maps were prepared on the cuts to compare the corresponding values of the image qualities and not only the displayed brightness. The properties of the mapped area are shown in table 6. Although the cuts were $20\ \mu m$ wide, the mapped area had to be smaller, because the shadow of the edges between the cuts which means we can get no diffraction pattern close to the sides.

The measured parameters are summarized in table 7 and values are plotted against

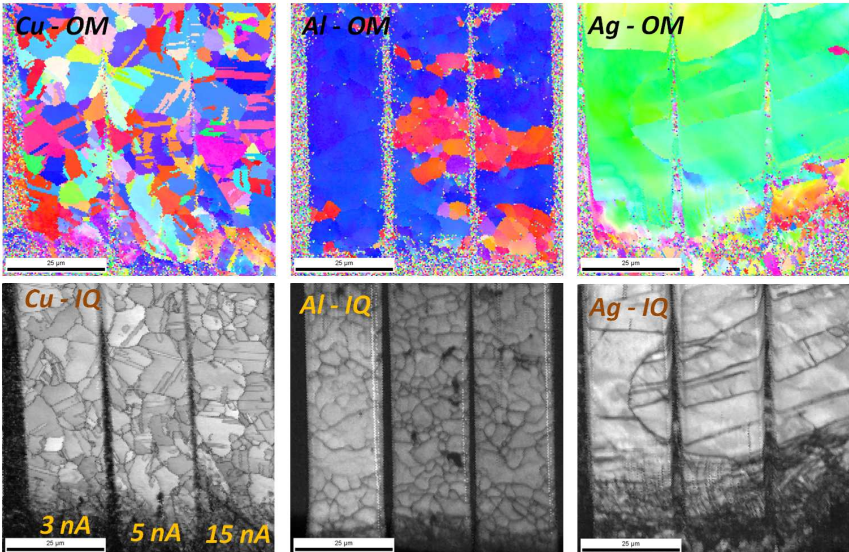

Figure 51: *Orientation maps made on the cuts prepared with FIB. The corresponding currents are shown in the figure*

the ion current in figure 52. The error bar showed on figure 52, is the largest error measured for Gentle Mill (table 10). FIB surface preparetion has much less source for errors, therefore, the deviations in the IQ cannot exceed the deviations calculated for Gentle Mill. The numbers in table 7 show the same as seen in images of figure 51 that in the case of copper, there is no change in IQ with increasing ion current, whereas Al and Ag show significantly higher IQ with $3\ nA$ than $15\ nA$.

The maps and the IQ values resulting from the FIB procedure are in the same range as the results we obtained when using the Gentle Mill (see later). It is very efficient and convenient that only stage movements are needed to start the measurement after preparing the surface. However, There are three rather disappointing disadvantages of

	Area ($\mu m \times \mu m$)	Step (μm)	Number of points
Cu	18×18	0.1	37725
Al	14×14	0.1	22761
Ag	15×15	0.1	26187

Table 6: *The mapped area for different materials*

the FIB preparation: cost, time and size:

- Gallium is quite expensive.
- Except for the copper, $3\ nA$ was needed to achieve the same result as with the Gentle Mill, which means that in order to get approximately $400\ \mu m^2$ valuable area, one has to work for more than an hour.
- In the IQ maps in figure 51, many grains can be seen on copper and aluminum and conclusions may be made concerning their microstructure. Silver, on the other hand, has far too large grains, thus, an area of this size will not give us adequate information.

Despite all of this, the lesson to be learnt is that FIB can be used very well for surface preparation, when the sample requires not to be transferred from instrument to instrument.

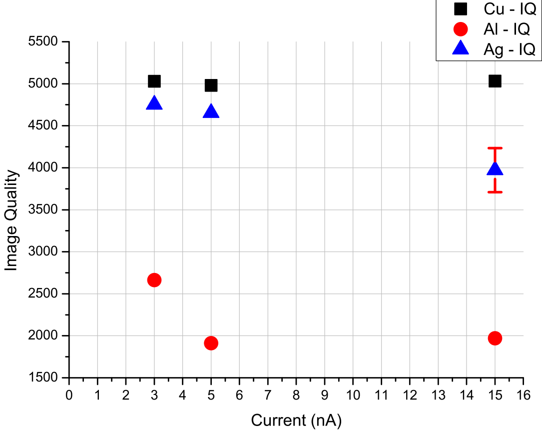

Figure 52: *Image quality as the function of ion current used for patterning*

I_{ion} (nA)	Cu IQ	Al IQ	Ag IQ
15	5032.38	1969.43	3971.61
5	4980.64	1912.51	4653.5
3	5029.17	2662.91	4750.47

Table 7: *The mapped areas for different materials*

3.2 Measurements Using Low Energy Argon Ion Beam - Gentle Mill

The Gentle Mill low energy argon ion polisher was designed, as its name indicates, gently remove the damaged, amorphous layer from the surface of transmission electron microscopy samples and has proven its usefulness in the past 28 years.

The surface requirements for EBSD investigation are very similar to the ones for TEM samples. Therefore, it seemed worth trying to test what the Gentle Mill is capable of in this field.

Figure 53: *Gentle Mill low energy ion polisher*

3.2.1 Polishing Method and Other Considerations

The Gentle Mill has four adjustable parameters: time of ion bombardment, accelerating voltage, angle of incidence and sample movement. Concerning the latter: ion polishing leaves marks on the sample which show the direction of incidence. To avoid this, the sample can be oscillated or rotated around the axis perpendicular to the surface. The maximum angle ($\pm 120°$) of the oscillation in the Gentle Mill is not large enough, so different areas of the surface will not be treated equally. This is inconvinient in case of the SEM, a relatively large area of the surface should be equally prepared, which can be achieved by rotating the sample.

Our specimens were not thoroughly polished, there were both scratches and holes on them previous to the Gentle Mill treatment. The goal was to smooth them as quickly as possible, thus, a lot of material had to be removed in a short time. This is why $1\ kV$ acceleration voltage seemed an appropriate choice.

Thus remained two parameters: time of polishment and angle of incidence. We changed these, looking for the optimum to get a good quality surface for EBSD.

The two setups are shown on figures 54 and 55.

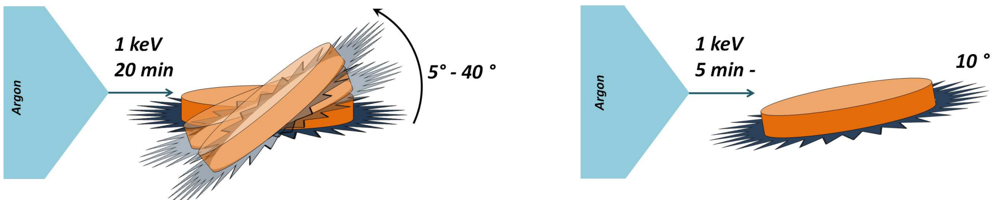

Figure 54: *Changing the angle of incidence*

Figure 55: *Changing the sputtering time*

First, the sample was fixed on the sample holder used in the Gentle Mill with conductive carbon tape. The depth of this sample holder can simply be adjusted manually with a screw, so that the height of the specimen could be set such that the beam could only reach the surface of it and not the sides. One has to use the naked eye for this procedure. After adjusting the height, the sample could be placed inside the instrument and polishing could take place. When this has been done, the sample holder needs to be changed and the specimen removed from the Gentle Mill's holder and mounted on the holder of the SEM. We did not use glue for this, because we experienced movements with carbon tape and the silver paint needed too much time to dry. Thus we designed a special holder, where a screw holds the sample in place.

As it can be seen in figure 51, the copper has more grains with different orientations per unit area than aluminum and silver. As it was mentioned before, the IQ parameter depends on the orientation. To get smaller deviation in the average IQ from the orientation dependence, more grains must be included in the map. Thus, the investigated area on silver and aluminum was twice as big as on copper. To not let the time of the measurement grow extremely, the step size between the measured spots was chosen to be double what it was in the case of copper. In table 8 these parameters are summarized and the sputtering rates of each material are shown also. Since the rate was calculated

with perpendicular incidence, it is not actually the sputtering rate of our measurements, but their relative value is important for us now.

	Area ($\mu m \times \mu m$)	Step (μm)	Number of points	Sputtering rate (atom/ion) [28]
Cu	40×40	0.2	46316	2.821
Al	80×80	0.4	46316	1.521
Ag	80×80	0.4	46316	3.688

Table 8: *The mapped areas and the sputtering rate for different materials. The sputtering rates were calculated for argon ions with* $1\ keV$ *energy and incidence perpendicular to the surface*

The changes in the surface topology are very unique for increasing angles of incidence and also for increasing sputtering time. Both measurements prove the statement that was mentioned in chapter 2.2.1, namely that sharp edges and peaks do not develop during ion sputtering.

3.2.2 Time Dependence

When changing the time of polishment, the angle of incidence was kept constant at $10°$. We started the measurements by polishing the sample for 5 minutes, then performing an orientation mapping, after which the same sample was put back in the Gentle

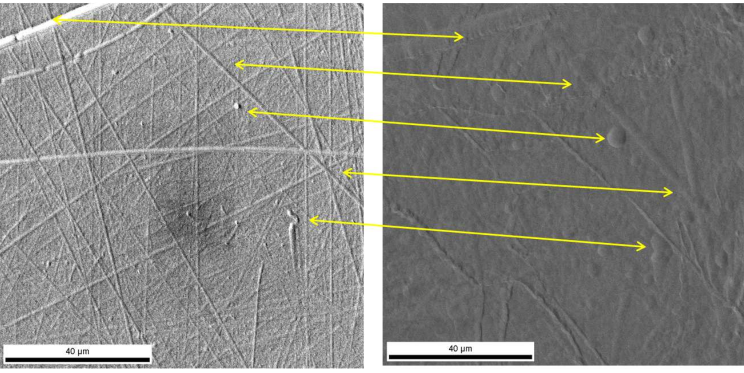

Figure 56: *Scratches and holes are getting wider on silver sample that was polished for 5 minutes (left) and 25 minutes (right) using* $1\ keV$ *energy argon at* $10°$ *angle of incidence*

Mill for additional 5 minutes. We continued this routine until we experienced a slight drop in the image quality. To confirm whether this drop was due to a random deviation or an actual surface degradation, an extra 10 minutes polishing was added. This proved to be a very useful routine. The orientation maps were taken on the same area of the surface after each time step, so that we could observe the changes in the topography.

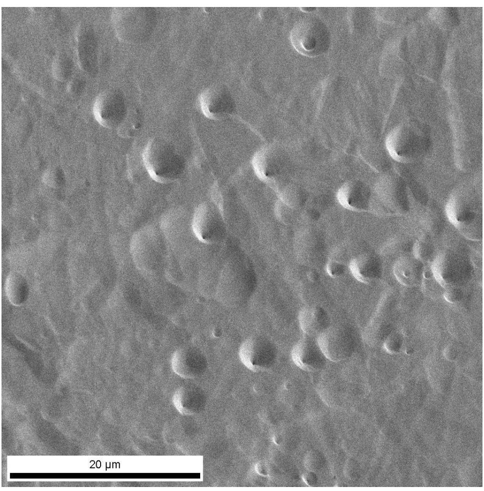

Figure 57: *Copper polished for 30 minutes, at* $10°$

When the time of the sputtering increases, the holes and scratches get wider and shallower. This supports the model described in chapter 2.2.1. The two walls of a scratch correspond to two steps, one on each side. Similar is true for the holes. The sputtering rate is increased on the edges, thus, they get less sharp and the wall of the scratch or the hole which is further from the ion source, moves away from the ion beam. The sample is rotated so that they get radiation equally from each direction, the wall which is further from the source, is always changing, so they start to move away from each other, this making the object wider. An example of this is shown for this in figure 56. On the left side an SEM image on a silver sample is shown: it was taken after polishing for 5 minutes at the angle of $10°$. On the right side, SEM image is shown that was taken after polishing for 25 minutes.

This effect is very well demonstrated in the case of copper. After ion polishing for 30 minutes, major craters evolved from the initial small holes (figure 57).

3.2.3 Angle Dependence

Unfortunately, the routine described in the previous chapter, 3.2.2, could not be followed when changing the angle of incidence. A new sample was used for every measurement, to ensure we always have the same initial surface. For the minimum angle of incidence $5°$ was chosen and we measured in $5°$ degree steps until the image quality started to drop. This was usually at $30°$ and therefore we did not need to go above this value. The time of polishment was kept on 20 minutes.

When the angle of incidence increases, the differences between the sputtering rates of the different orientations also increases and around $15°$ becomes noticeably strong. This effect is the most obvious on the copper samples, but can be observed on silver too and slightly on aluminum. On the left of figures 58, an orientation map obtained on copper is shown. The angle of incidence of the $1\ keV$ energy argon beam was $30°$ and the time of polishment was 20 minutes. On the right side, an SEM image of the mapped area can be seen. Observe the differences in the topography.

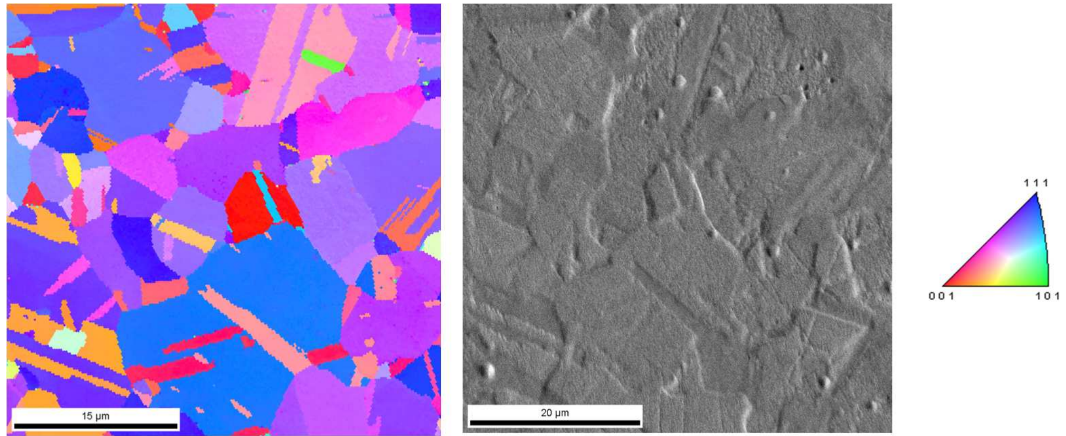

Figure 58: *Differential sputtering on copper polished with $1\ keV$ energy argon at $30°$ angle of incidence for 20 minutes*

3.2.4 Results and Discussion of EBSD Measurements

From investigating the surface of the samples after ion polishing, the conclusion is that after a certain time, the surface will be far too damaged for EBSD. An EBSD surface can not have major craters like the ones seen on copper in figure 72 or even on

silver in figure 80, because even if there is diffraction and there is no shadowing, the angle of the surface is not homogeneous, there are large deviations from the 70° tilt.

Concerning the angle of incidence: it would be preferable to polish the samples at glancing ion incidence, but that is only efficient, if the sample was properly polished before, which we wish to avoid. 5° is far from glancing incidence and yet the sputtering rate was not high enough to completely remove the damaged surface in 20 minutes.

In other words, we have to make a compromise. We have to find the angle of incidence, where the differential sputtering due to the orientation differences is not too strong and the time of the sputtering does not make the defects on the surface grow to extremely large sizes.

We plotted the average IQs against the sputtering time and the angle of incidence. These graphs are shown in appendix A, with the actual parameters summarized in tables 11 and 12. Besides the image qualities the average confidence indices are displayed too. Remember that only the IQ parameter has any connection with the surface, the CI only provides information on how trustworthy the orientation data is.

One can observe that IQ as well as the CI attains a saturation value (figure 59). One exception is in the angle dependence of the aluminum, where the CI parameter rapidly drops by two tenths (figure 60).

Before explaining this phenomena, let us have a look on the orientation maps and image qualities in appendix B. That we have a maximum in the IQ parameter for a

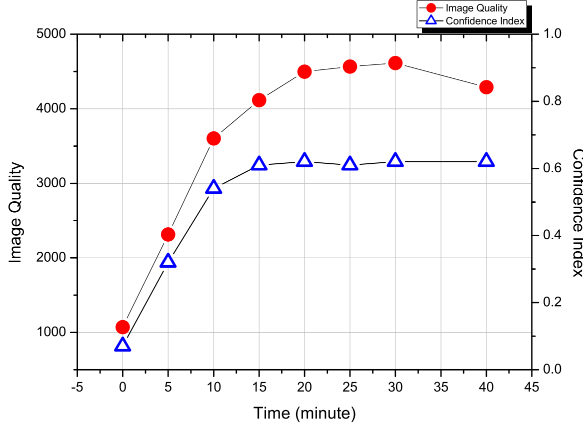

Figure 59: *Silver polished for different times*

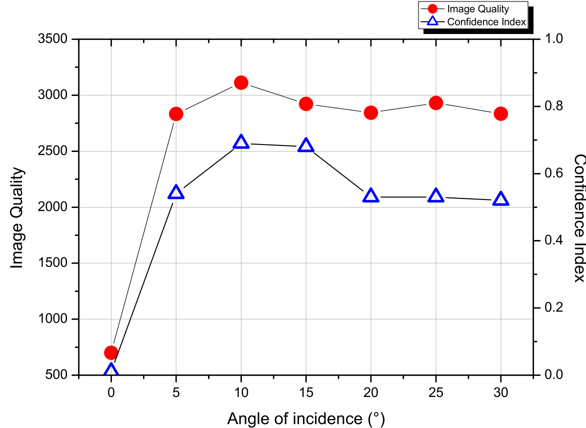

Figure 60: *Aluminum polished under different angle of incidences*

certain angle of incidence and for a certain polishing time does not necessary mean that the orientation map we got has high quality.

We can observe that when the incidence angle of the argon ion beam is $5°$ or the polishing time 5 minutes, the scratches do not disappear and they disturb the orientation mapping. They are obvious not only on the image quality map, where they appear much darker than average, but they are also visible on the orientation maps. This means that false information is provided from the points of these scratches. In figures 71 ($5°$) and 77 (5 min) a deep scratch appears with many colours on the OM. When something like this is seen on an OM, one has to be suspicious. Most probably a proper diffraction pattern is not recorded from that area.

Increasing the angle of incidence or the time of polishing, the flaws corresponding to the defects on the surface disappear first from the orientation maps, then by further increasing these parameters, they smoothen on the image quality map too (figure 61).

	Angle of incidence (°)	Time of polishing (min)
Copper	15	20
Aluminum	10	15
Silver	10	30

Table 9: *Angle of incidence and time of polishing corresponding to the maximum image quality*

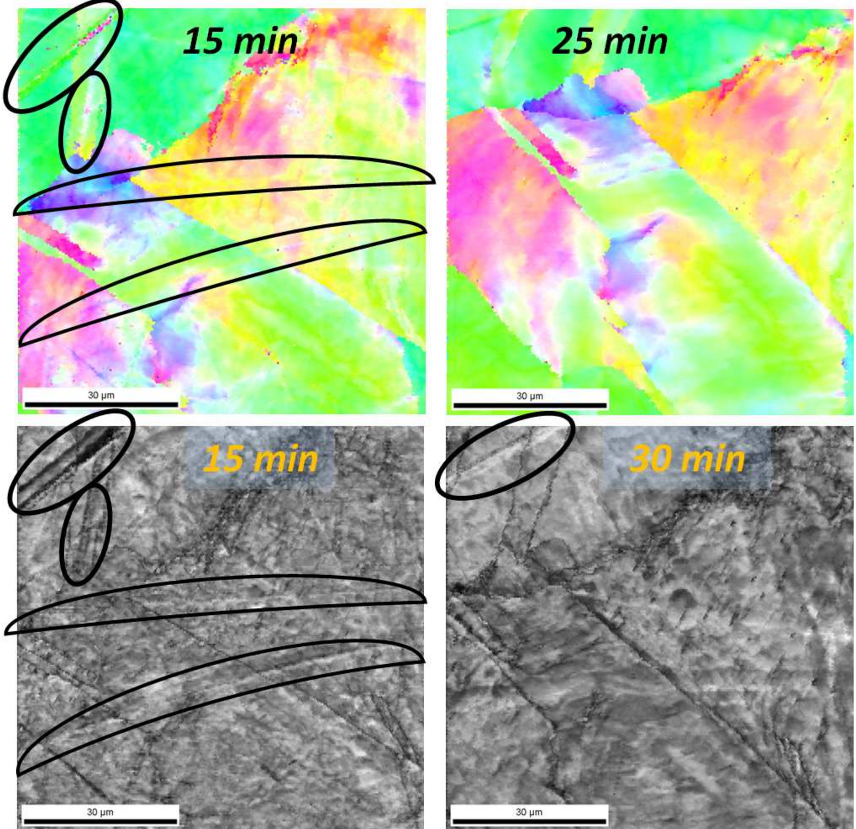

Figure 61: *Scratches disappearing from the OM and smoothening on the IQ map (Ag sapmle polished under* 10°*)*

At this point, we get the maximum average IQ. The OM corresponding to this point has a very good quality. The time of polishing and the angle of incidence where the best IQs was measured are summarized in table 9.

Aluminum

The investigation of copper was very straightforward, as the measured IQ points fit on a smooth curve and there are no big deviations in them (figures 64 and 65). Aluminum and silver on the other hand behaves strangely. As mentioned before, the CI parameter of Al drops rapidly from one angle to the other and on the orientation maps one can see spots with too many colours to be considered reliable. Indeed, the orientation measured in these areas are not valid. Also, there are black spots on the IQ maps

corresponding to these colourful areas. The reason is simple. Our sample was not pure aluminum: it was industrial aluminum, containing magnesium, silicon and manganese impurities. In fact, manganese is present in the form of relatively large inclusions. These are the bright spots seen in figures 74 and 76. Of course, the diffraction patterns calculated for aluminum will not fit the diffraction pattern recorded from the manganese inclusions. This destroys the values of IQ and CI at those points. As a result, there are larger relative errors in the average IQs measured on aluminum (table 10).

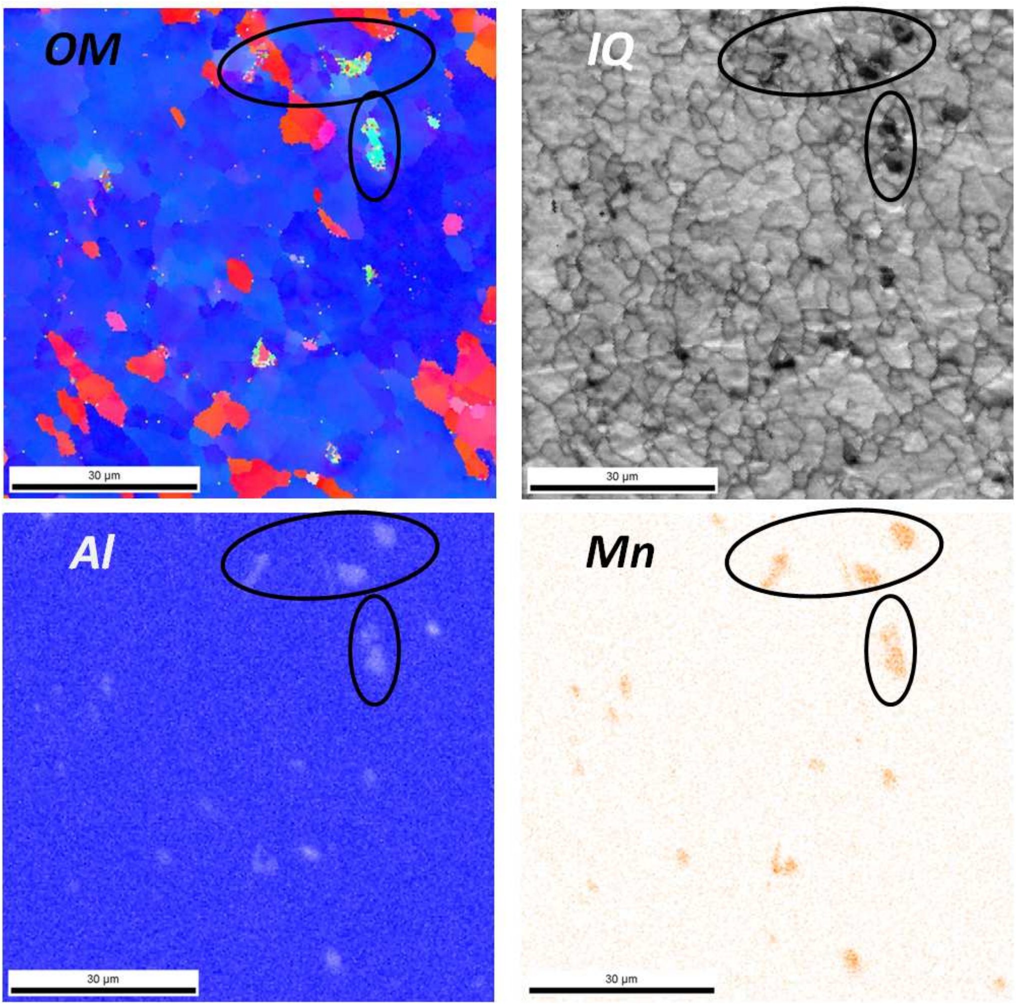

Figure 62: *OM and IQ maps and maps of the Al and Mn concentration. The false orientations corresponds the higher Mn concentrations*

In order to prove the discussion above, element maps were also prepared by collecting X-rays from each point. In figure 62, IQ, OM and element maps are shown. The

surface was polished with a $1\ keV$ energy argon ion beam with angle of incidence of $10°$ for 20 minutes. It is clearly visible that the spots of false orientations correspond to the higher manganese concentrations.

Silver

The situation with the silver is a slightly more complicated. The development of the surface is much slower than it is for the aluminum and for the copper, although it has much higher sputtering rate. Despite the fact that thicker layers are removed from the surface, the diffraction patterns do not improve faster. They have a very low quality after sputtering for 5 minutes and also when the angle of incidence was $5°$ degrees. This suggests that Ag is covered with a thick damaged layer. The question is why is this layer so damaged.

Diamond paste is not suggested for surface polishing when EBSD investigation is the goal, because it is well known to deform the surface. Despite this, we did use diamond paste, because the deformed surface was to be removed using the Gentle Mill. It is highly possible that the silver sample was damaged deep under the surface during mechanical polishing however, and therefore more material would need to be removed to see diffraction patterns.

This assumption is supported by the the work of J. Gubicza et al., in reference [30]. They show that the average dislocation density in the saturation state of silver is more than twice as high as it is in copper and an order higher then aluminum. This is due to the fact that silver has very low stacking fault energy.

After removing the damaged layer from the surface of the silver, another curiosity remains, namely, that in figures 79 and 81, the colours in the orientation maps look like watercolours in the rain. The slight shade changes inside a monocoloured area suggest that plastic deformations are present in the material. The plastic deformations result in lattice rotation, which in metals is typically several degrees. EBSD's misorientation resolution in general is in the order of $0.5°$, but with direct pattern analysis methods this can be improved to even $0.01°$. In other words, EBSD is a very sensitive tool for the investigation or intragranual misorientations [29]. As in the case of orientation and image quality, we can also map the deviations from chosen orientation. In figures 63 Grain Reference Orientation Deviation Maps are shown for silver, ion polished for 15

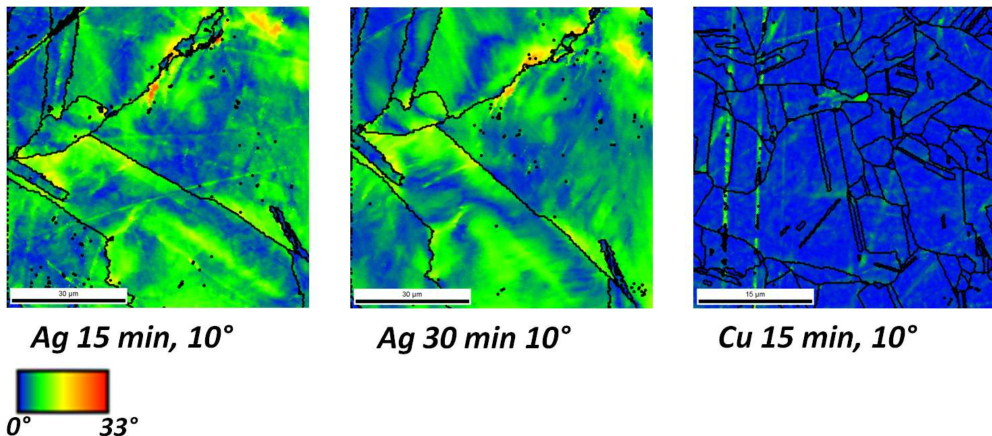

Figure 63: *Grain Reference Orientation Deviation Maps obtained on Ag (15 minutes,* $10°$*), Ag (30 minutes,* $10°$*) and Cu (15 minutes,* $10°$*) respectively. The grain boundaries are shown with black lines. Note the differences between the two materials. The two maps on the silver were taken on the same area. Note also the changes in the deviation angles, thus the changes in the dislocation density.*

minutes $(1\ keV,\ 10°)$, for 30 minutes $(1\ keV,\ 10°)$ and copper, ion polished for 15 minutes $(1\ keV,\ 10°)$. On these maps the chosen orientation is the average orientation of each grain. The colours correspond to the angle between the measured orientation at the point and average orientation of the grain, where the point belongs. Note that the silver has very high angles of deviation compared to the copper, which hardly shows any. The lattice distortion showed in figures 63 was caused by deformations during the history of the sample.

There are many contributions to the deviations observed in the measurements on all our samples, the most important of which are:

- The orientation dependence of the image quality
- When adjusting the height of the sample in the Gentle Mill's sample holder, one has to rely on the naked eye, which can cause deviations
- Surface topology
- Contaminations
- Inclusions from foreign material

Probably it is impossible to give a complete list of these, but to be able to give an estimate of the error induced by all possible sources, even the ones we did not think of, we measured twice at a given point. The results of these measurements are summarized in table 10. The relative deviations are fairly similar, as it would expected, and the highest for the aluminum because of the manganese inclusions.

<table>
<tr><th></th><th colspan="2">Copper</th><th colspan="2">Aluminum</th><th colspan="2">Silver</th></tr>
<tr><td>Conditions</td><td colspan="2">1 keV, 10°, 20 min</td><td colspan="2">1 keV, 10°, 20 min</td><td colspan="2">1 keV, 10°, 40 min</td></tr>
<tr><td>IQ</td><td>5015.83</td><td>4492.03</td><td>3112.33</td><td>2672.27</td><td>4290.18</td><td>3963.93</td></tr>
<tr><td>Average IQ</td><td colspan="2">4753.93</td><td colspan="2">2892.3</td><td colspan="2">4127.055</td></tr>
<tr><td>Statistical error</td><td colspan="2">261.9</td><td colspan="2">220.03</td><td colspan="2">163.125</td></tr>
<tr><td>Relative error</td><td colspan="2">0.055</td><td colspan="2">0.076</td><td colspan="2">0.039</td></tr>
</table>

Table 10: *Average deviation and relative errors for the different materials*

4 Conclusion

We have showed that both FIB and the Gentle Mill were able to prepare a quality surface on which high quality EBSD mapping could be performed.

The initial surfaces of our samples were roughly polished, and contained many scratches. After many initial, unsuccessful attempts to obtain diffraction pattern, it was rather surprising for us that we were able to observe Kikuchi bands from a surface only ion polished for a few minutes with relatively high energy ions.

We were able to find angles of incidences and a polishing times for all of our investigated materials, where we could see no signs of defects on the OMs nor on the IQ maps. The optimum angle and time values are summarized in table 9. Using these parameters for copper, aluminum and silver with similar initial surfaces will result in similar quality measurements.

There are only two inconveniences when using the Gentle Mill versus the FIB, namely that the sample has to be transferred from instrument to instrument, and that one has to change sample holder. In some cases, this is a danger to the sample, and we can easily harm the surface. In addition to characterising the ideal preparation parameters for the Gentle Mill, we have provided a recipe for sample preparation using FIB. In this case, only stage movements are required to move from preparation to investigation. This procedure is very convenient, however, it is time consuming, expensive, and only a small area can be investigated.

Based on our measurements, the Gentle Mill is a nearly perfect tool for surface preparation for EBSD. We aim to continue this work as follows:

- Test whether it is possible to get a smooth surface from a roughly polished one only using an argon ion beam, and discover how time consuming it would be and investigate the effects of different energy beams.
- Extending the range of the investigated materials with insulators, geological samples.
- Using an instrument also designed by Technoorg Linda Ltd. Co. with a higher energy argon ion gun, which can be used to prepare cross sections with smooth surfaces. Question is in which cases can this instrument be used instead of the FIB.

A Appendix

Angle of incidence	Cu IQ	Al IQ	Ag Iq
Mechanically polished = 0	841.65	700.15	1071.67
5	3883.65	2832.15	2471.27
10	4492.03	3112.33	4788.44
15	4925.52	2922.79	4319.58
20	4803.18	2843.00	4228.95
25	4560.25	2931.57	-
30	4325.48	2835.26	4447.18

Table 11: *Average IQ parameters measured in different angles*

Time (minute)	Cu IQ	Al IQ	Ag Iq
Mechanically polished = 0	841.65 0	700.15	1071.67
5	2836.95	2398.11	2314.57
10	3888.05	2728.66	3601.24
15	4419.99	2747.85	4114.86
20	5015.83	2672.27	4497.39
25	4668.47	-	4566.85
30	4399.85	-	4613.95
40	4336.29	-	4290.18

Table 12: *Average IQ parameters measured for different polishing times*

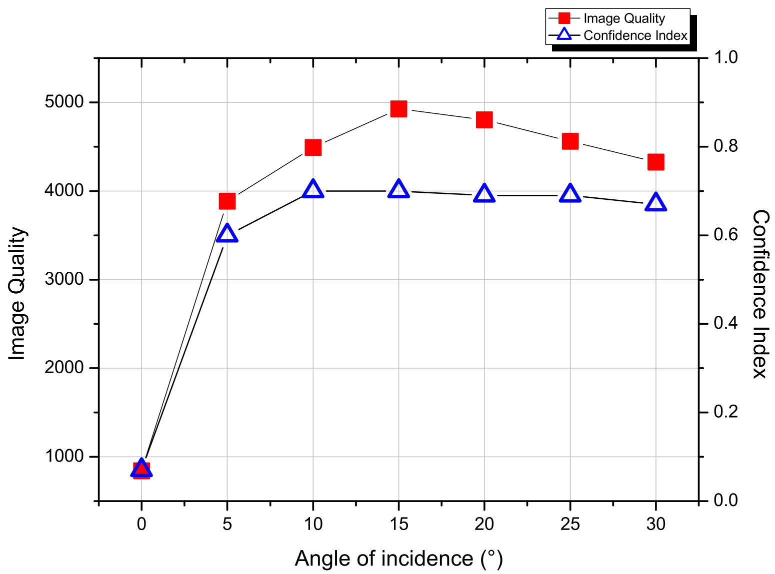

Figure 64: *Copper polished under different angle of incidences*

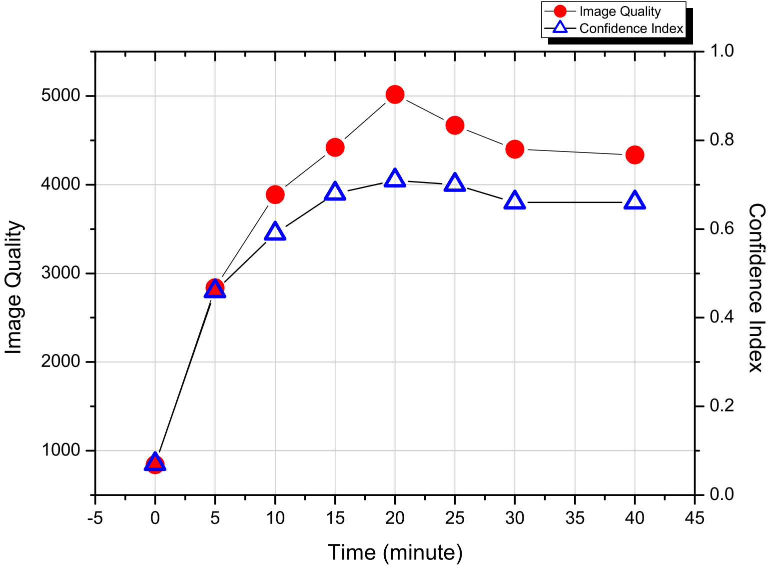

Figure 65: *Copper polished for different times*

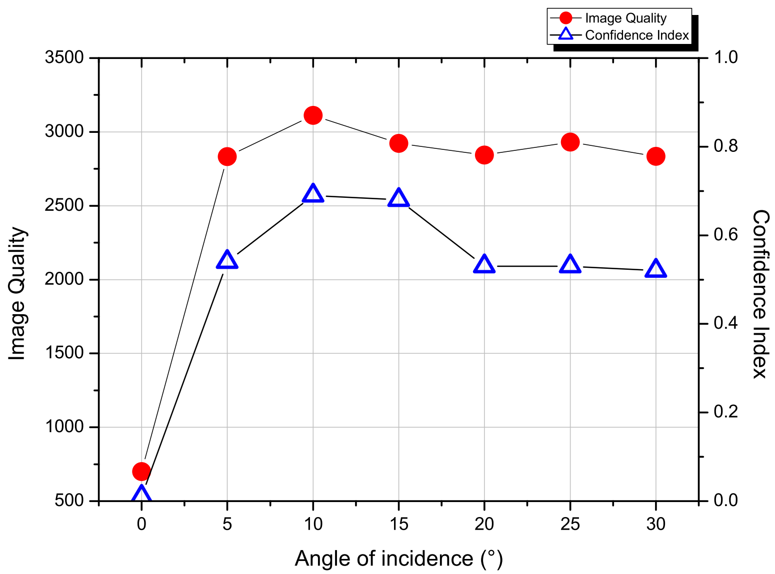

Figure 66: *Aluminum polished under different angle of incidences*

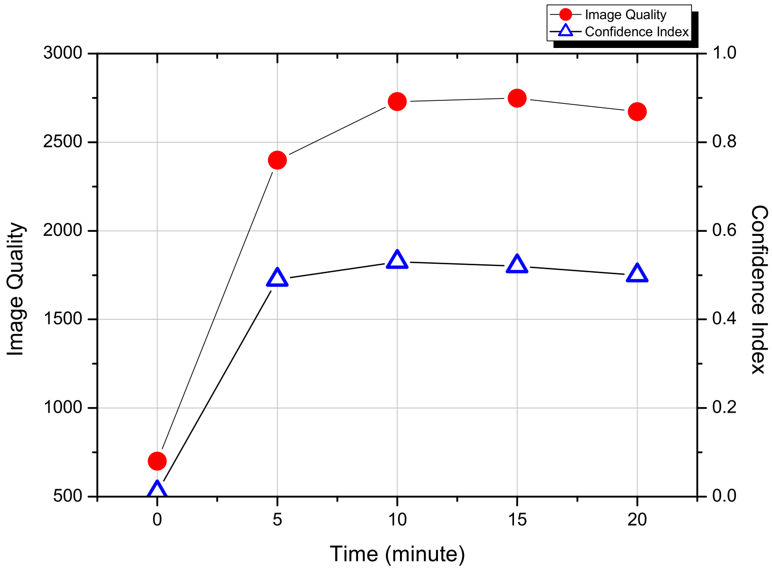

Figure 67: *Aluminum polished for different times*

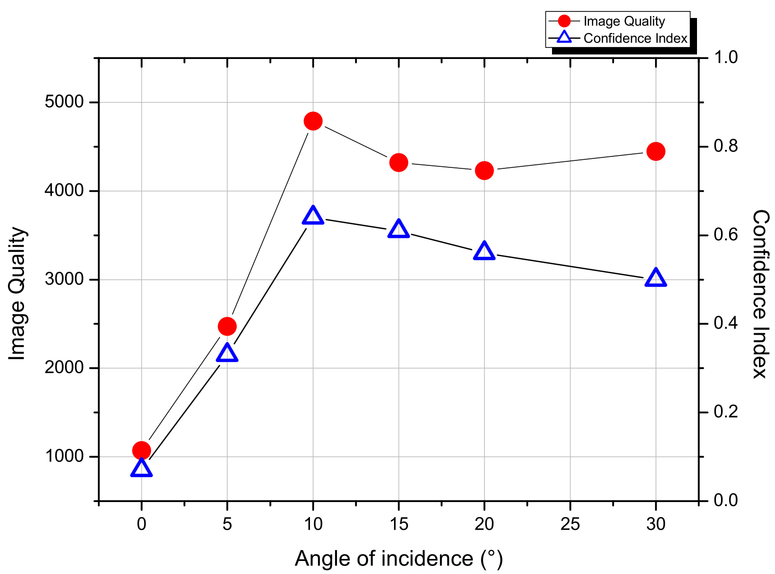

Figure 68: *Silver polished under different angle of incidences*

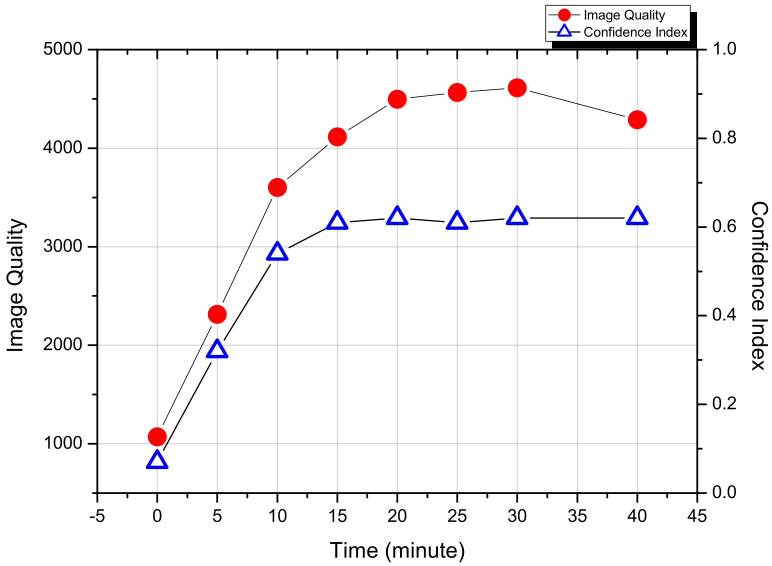

Figure 69: *Silver polished for different times*

B Appendix

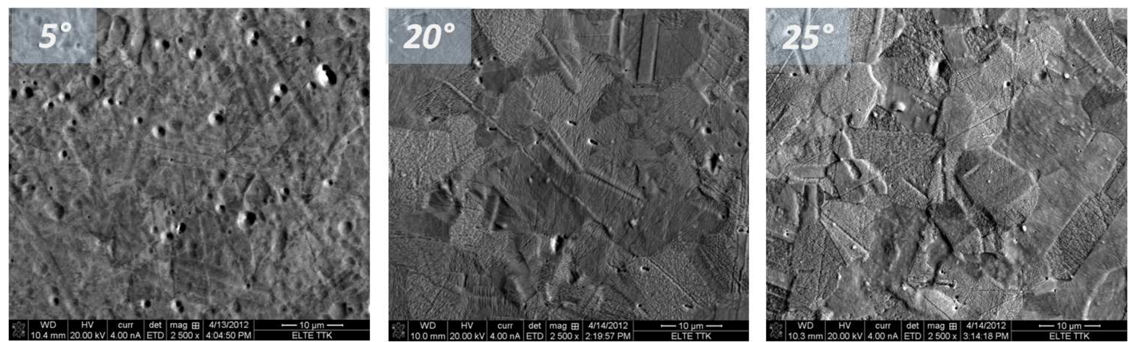

Figure 70: *Surface changes on copper when polished under different angles*

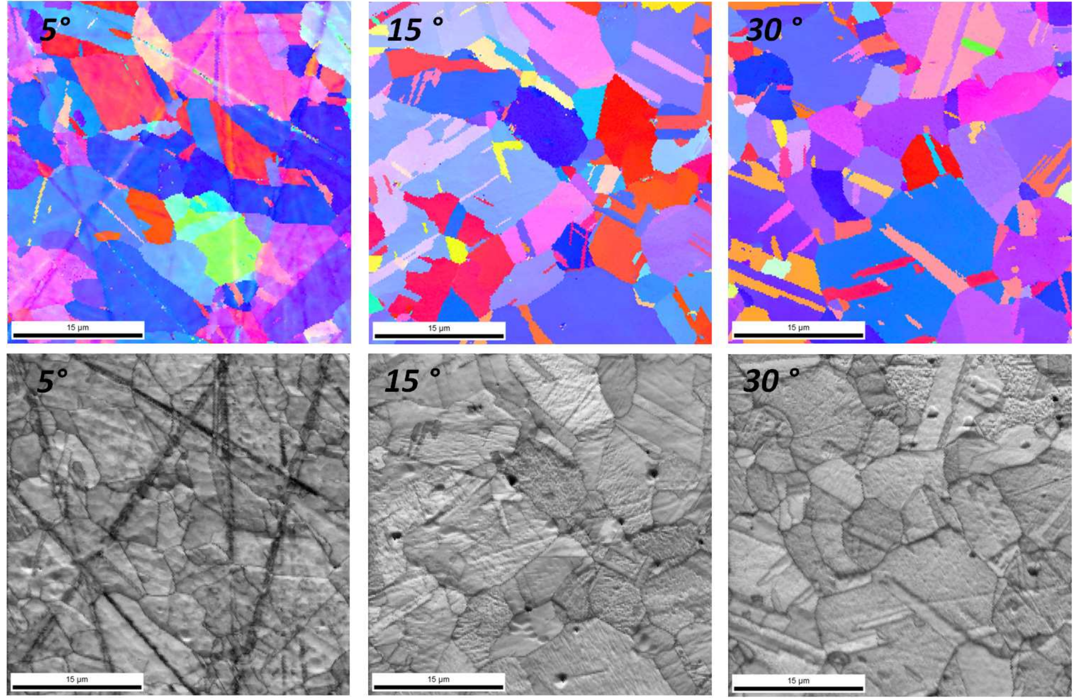

Figure 71: *Changes of the OMs and IQ maps of copper when polished under different angles*

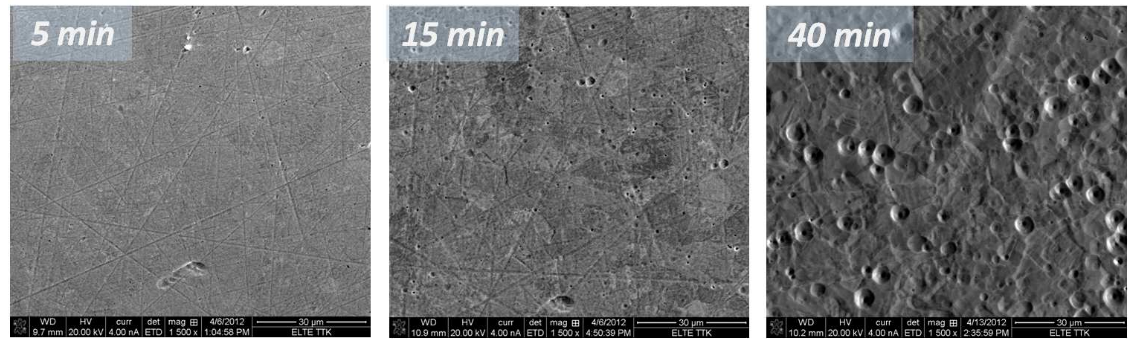

Figure 72: *Surface changes on copper when polished for different times*

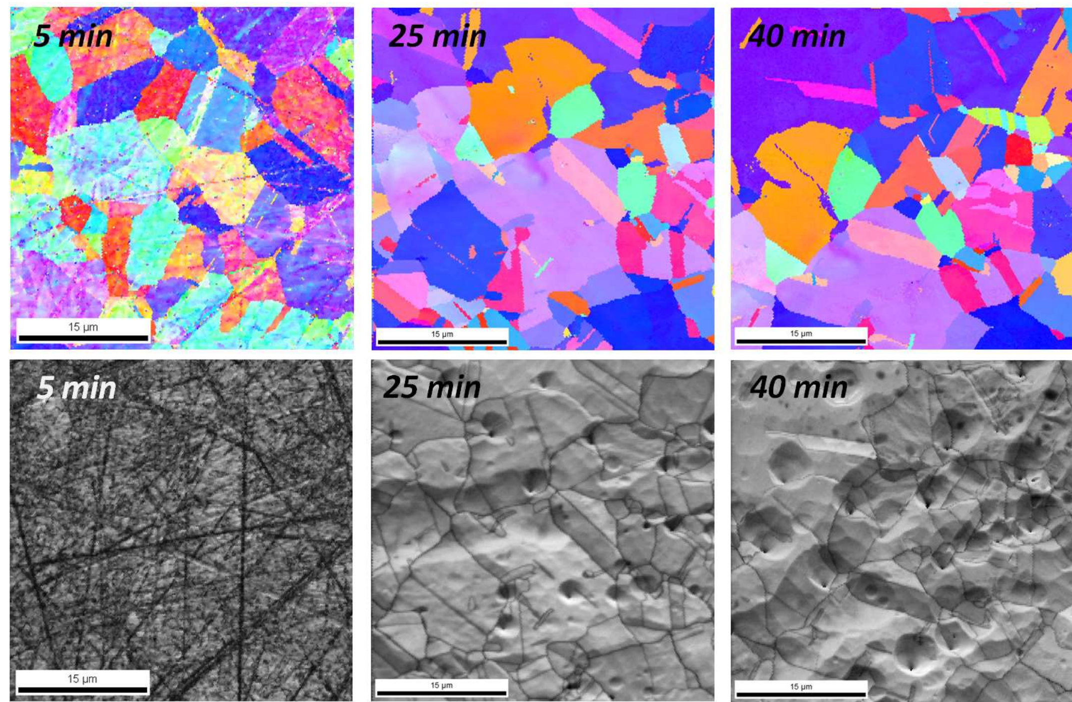

Figure 73: *Changes of the OMs and IQ maps of copper when polished for different times*

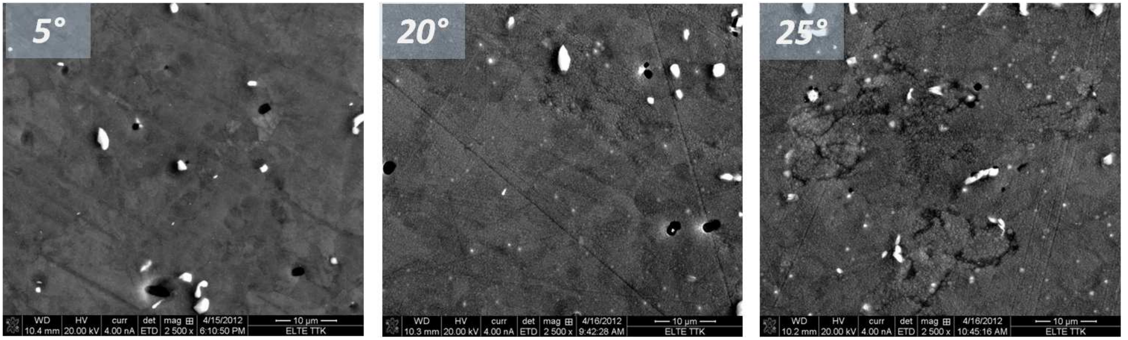

Figure 74: *Surface changes on aluminum when polished under different angles*

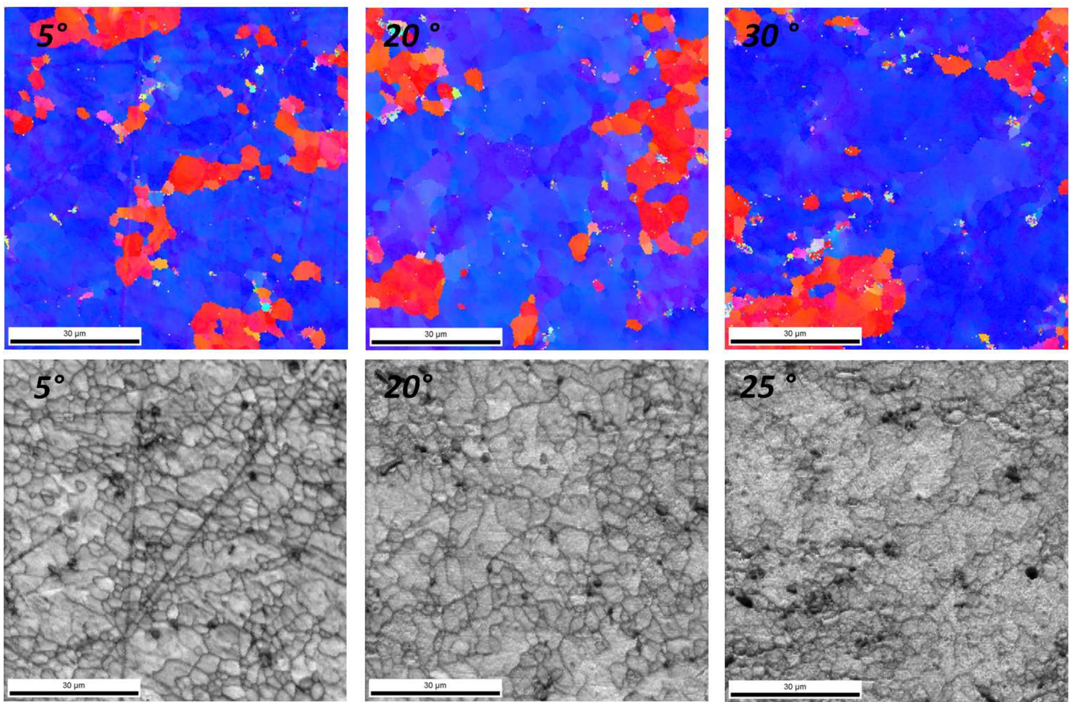

Figure 75: *Changes of the OMs and IQ maps of aluminum when polished under different angles*

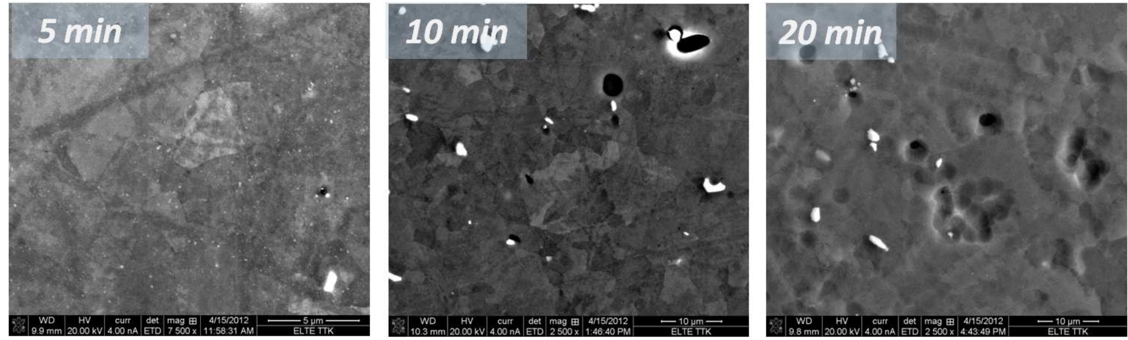

Figure 76: *Surface changes on aluminum when polished for different times*

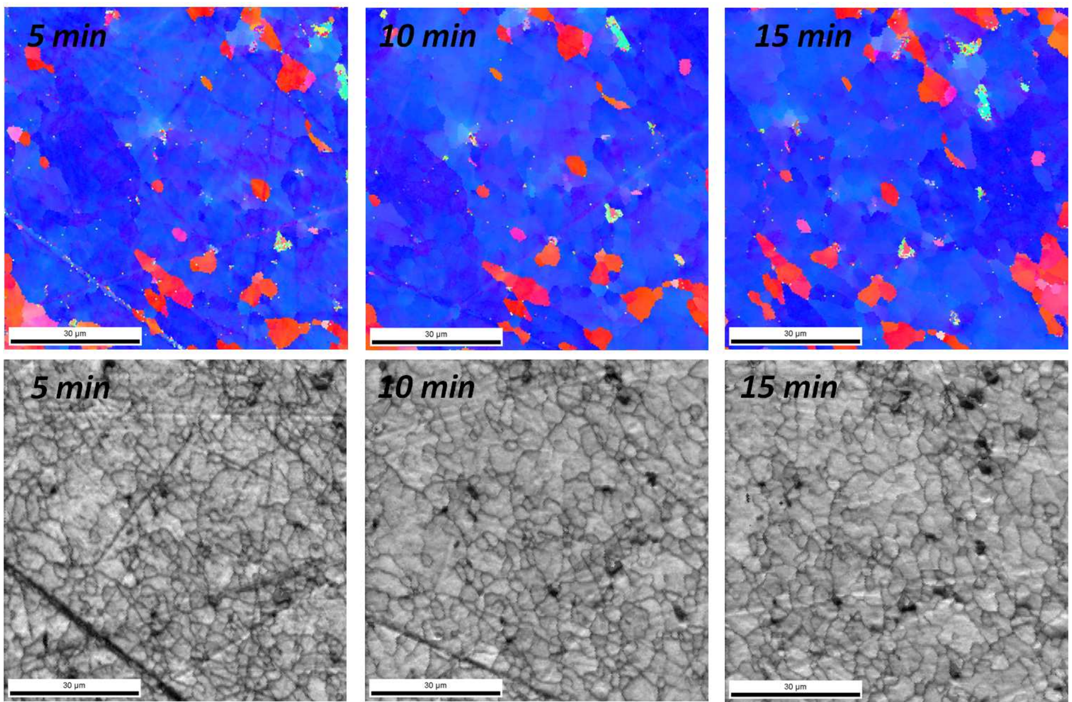

Figure 77: *Changes of the OMs and IQ maps of aluminum when polished for different times*

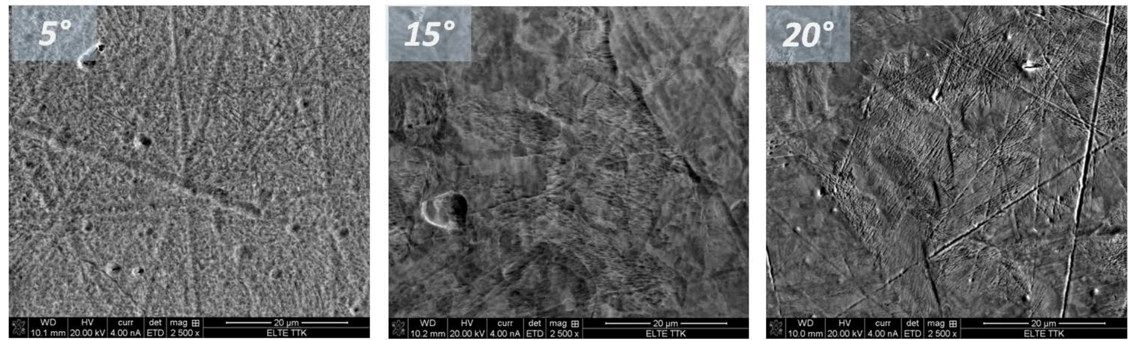

Figure 78: *Surface changes on silver when polished under different angles*

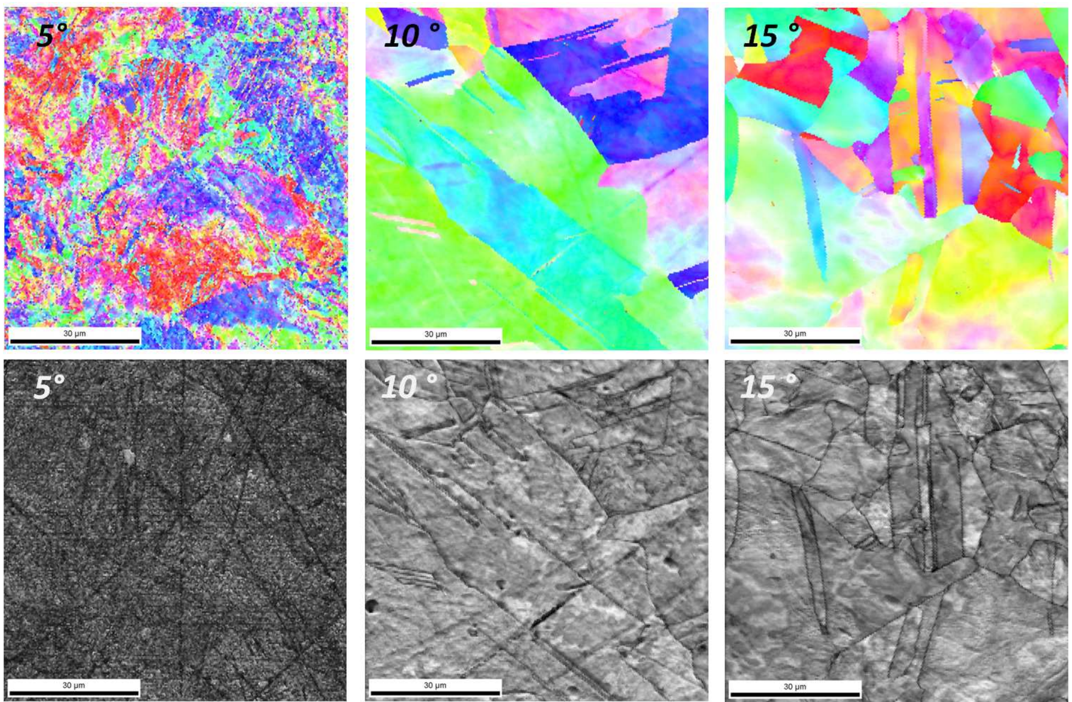

Figure 79: *Changes of the OMs and IQ maps of silver when polished under different angles*

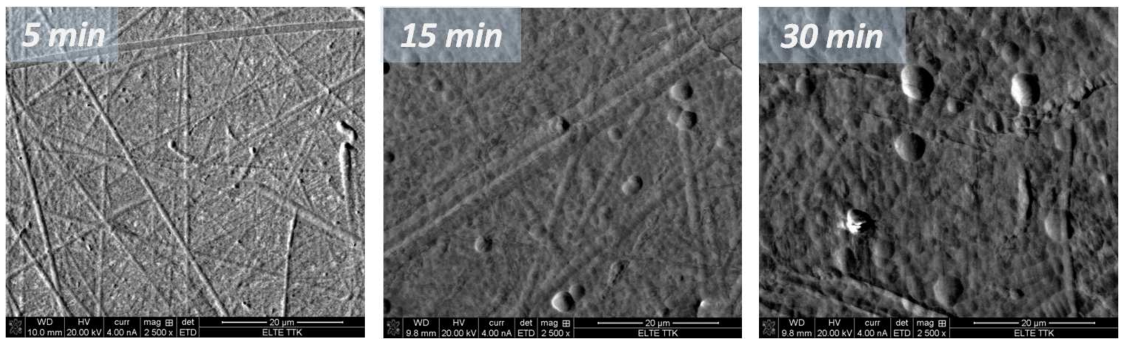

Figure 80: *Surface changes on silver when polished for different times*

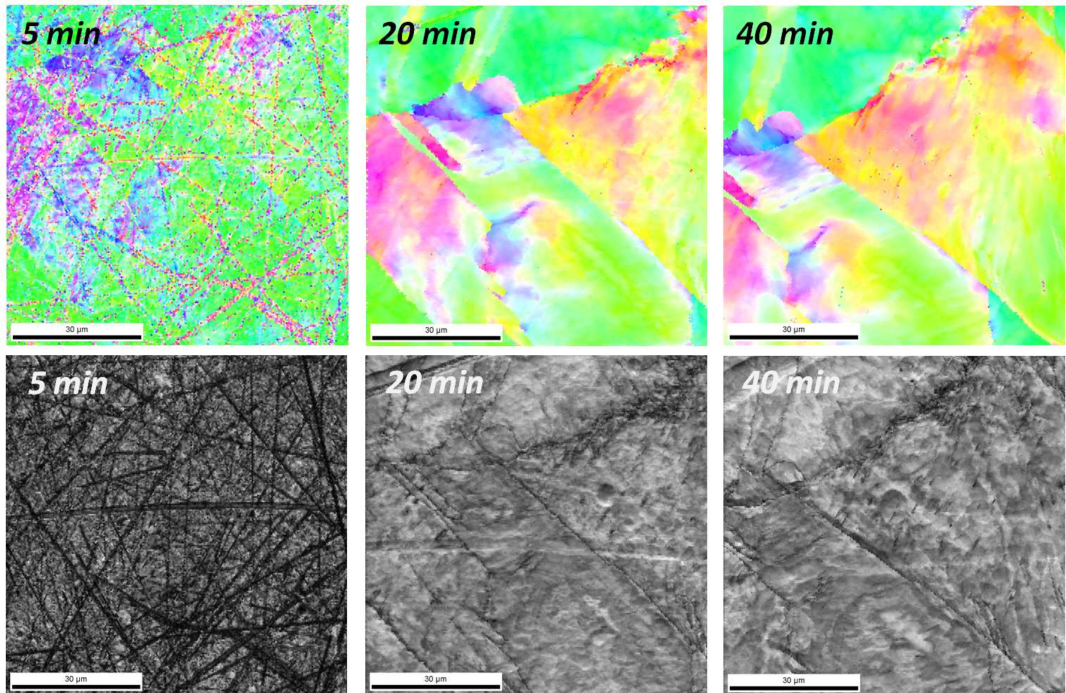

Figure 81: *Changes of the OMs and IQ maps of silver when polished for different times*

References

[1] O. Engler, V. Randle: Introduction to Texture Analysis - Macrotexture, Microtexture, and orientation mapping, CPC Press (2010)

[2] S. Nishikawa, S. Kikuchi: Diffraction of Cathode Rays by Calcite, Nature, **122**(1928) 726

[3] Boersch: About bands in electron diffraction, Physikalische Zeitschrift, **38** (1937) 1000

[4] M. N. Alam, M. Blackman, D. W. Pashley: High-Angle Kikuchi Patterns, Proc. Roy. Soc., **221** (1954) 224.

[5] J. A. Venables and C. J Harland: Electron back-scattering patterns - A new technique for obtaining crystallographic information in the scanning electron microscope, Philosophical Magazine, **27** (1973) 1193.

[6] D. J. Dingley: On-line determination of crystal orientation and texture determination in an SEM, Proc. Roy. Microsc. Soc., **19** (1984) 74.

[7] T. Maitland, S. Sitzman: Electron Backscatter Diffraction (EBSD) Technique and Materials Characterization Examples, Scanning Microscopy for Nanotechnology, Edited by W. Zhou, Z. L. Wang, Springer (2006)

[8] `http://www.purdue.edu/rem/rs/graphics/sem2.gif`

[9] Source of the figure: Rudolf Reichelt: Scanning Electron Microscopy, Science of Microscopy, Edited by Peter W. Hawkes, John C.H. Spence, Volume I, Springer (2007)

[10] F.A. Stevie, L.A. Giannuzzi, B.I. Prenitzer: The Focused Ion Instrument, Introduction to Focused Ion Beams - Instrumentation, Theory, Techniques and Practice, Edited by Lucille A. Giannuzzi, Fred A. Stevie, Springer (2005)

[11] L.A. Giannuzzi, B.I. Prenitzer, B.W. Kempshall: Ion-Solid Interactions, Introduction to Focused Ion Beams - Instrumentation, Theory, Techniques and Practice, Edited by Lucille A. Giannuzzi, Fred A. Stevie, Springer (2005)

[12] T.L. Matteson, S.W. Schwarz, E.C. Houge, B.W. Kempshall, L.A. Giannuzzi: Electron Backscattering Diffraction Investigation of Focused Ion Beam Surfaces, Journal of Electronic Materials **31** (2002) 33

[13] R. J. Young, M. V. Moore: Dual-beam (FIB-SEM) Systems, Techniques and Automated Applications, Introduction to Focused Ion Beams - Instrumentation, Theory, Techniques and Practice, Edited by Lucille A. Giannuzzi, Fred A. Stevie, Springer (2005)

[14] Chapter is based on and the source of the figures: Gentle Mill 3 Ion Mill Model IV8, IV8HI for endpolishing TEM (Transmission Electron Microscopy) samples with a low energy ion gun - Technical Manual v3.2

[15] Á. Barna, G. Radnóczi, B. Pécz: Preparation Techniques for Transmission Electron Microscopy, Handbook of Microscopy - Application in Materials Science, Solid-State Physics and Chemistry (Applications), Edited by S. Amelinckx, D. van Dyck, J. van Landuyt, G. van Tendeloo, VCH (1997)

[16] Á. Barna, P. B. Barna, A. Zala: Ion Beam Induced Roughness and its Effect in AES Depth Profiling of Multilayer Ni/Cr Thin Films, Surface and Interface Analysis **12** (1988) 144

[17] H. E. Roosendaal: Sputtering Yields of Single Crystalline Targets, Topics in Applied Physics, Edited by R. Behrisch **47** Springer (1981) 219

[18] W. H. Bragg, W. L. Bragg: The Reflection of X-rays by Crystals, Proc. R. Soc. Lond. A **88** (1913) 428

[19] L. Reimer: Scanning Electron Microscopy - Physics of Image Formation and Microanalysis, Springer (1998)

[20] R. A. Schwarzer, D. P. Field, B. L. Adams, M. Kumar, A. J. Schwartz: Present State of Electron Backscatter Diffraction and Prospective Developments, Electron Backscatter Diffraction in Materials Science, Edited by A. J. Schwartz, M. Kumar, B. L. Adams, D. P. Field, Springer (2009)

[21] N. C. Krieger Lassen, D. J. Jensen, K. Conradsen: Image processing procedures for analysis of electron back scattering patterns, Scanning Microscopy **6** (1992) 115

[22] K. Kunze, S. I. Wright, B. L. Adams, D. J. Dingley: Advances in Automatic EBSP Single Orientation Measurements, Textures Microstructures **20** (1993) 41

[23] J. Radon: Über die Bestimmung von Funktionen durch ihre Integralwerte längs gewisser Mannigfaltigkeiten, Ber. Sächs. Akad. Wiss. Leipzig Math.-Phys. Klasse **69** (1917) 262

[24] EDAX-TSL OIM 5.3 Manual

[25] S.T. Wardle, L. S. Lin, A. Cetel, B.L. Adams: Orientation Imaging Microscopy: Monitoring Residual Stress Profiles in Single Crystals using an Image-Quality Parameter, IQ, Proceedings 52nd Annual Meeting of the Microscopy Society of America, Edited by G. W. Bailey, A.J. Garratt-Reed, San Francisco Press: San Francisco (1994)

[26] `http://www.dl.ac.uk/MEIS/stereographs/sp.fcc.100.html`

[27] Krishna Rajan: Representation of Texture in Orientaton Space, Electrom Backscatter Diffraction in Materials Science, Edited by A. J. Schwartz, M. Kumar, B. L. Adams, Kluwer Academic/Plenum Publishers (2000)

[28] `http://www.iap.tuwien.ac.at/www/surface/sputteryield`

[29] L. N. Brewer, D. P. Field, C. C. Merriman: Mapping and Assessing Plastic Deformation Using EBSD, Electron Backscatter Diffraction in Materials Science, Edited by A. J. Schwartz, M. Kumar, B. L. Adams, D. P. Field, Springer (2009)

[30] J. Gubicza, N. Q. Chinh, J. L. Lábár, Z. Hegedűs, C. Xu, T. G. Langdonc: Microstructure and yield strength of severely deformed silver, Scripta Materialia **58** (2008) 775